

**SILICON-GERMANIUM BIPOLAR TECHNOLOGY FOR ENABLING  
COLD-CAPABLE, RADIATION-TOLERANT ELECTRONICS FOR  
SPACECRAFT**

A Thesis Proposal  
Presented to  
The Academic Faculty

By

George N. Tzintzarov

In Partial Fulfillment  
of the Requirements for the Degree  
Master of Science in the  
School of Electrical and Computer Engineering

Georgia Institute of Technology

August 2020

Copyright © George N. Tzintzarov 2020

**SILICON-GERMANIUM BIPOLAR TECHNOLOGY FOR ENABLING  
COLD-CAPABLE, RADIATION-TOLERANT ELECTRONICS FOR  
SPACECRAFT**

Approved by:

Dr. John D. Cressler, Advisor  
School of Electrical and Computer Engineering  
*Georgia Institute of Technology*

Dr. Nelson Lourenco  
School of Electrical and Computer Engineering  
*Georgia Institute of Technology*

Dr. Azedah Ansari  
School of Electrical and Computer Engineering  
*Georgia Institute of Technology*

Date Approved: July 24, 2020

For in much wisdom, is much vexation, and he who increases knowledge increases sorrow.

*Ecclesiastes 1:18*

For now we see in a mirror dimly, but then face to face. Now I know in part; then I shall know fully, even as I have been known.

*1 Corinthians 13:12*

He determines the number of stars; he gives to all of them their names.

*Psalms 147:4*

*To my beloved Lord and Father in Heaven  
who breathes life into me and shows me the  
greatest love I have ever known.*



## ACKNOWLEDGEMENTS

I would first like to thank my research advisor Dr. John D. Cressler for his unwavering support not only in my academic career as a mentor, but also in my personal life as a friend and someone I can trust when things just do not line up. I am extremely grateful for all of the lessons he has taught me and his continued determination to make me a successful researcher.

I would also like to thank the members of my reading committee Dr. Azadeh Ansari and Dr. Nelson Lourenco. I am thankful that you would spend the time reading through this lengthy thesis, providing feedback, and making me better for it. I would also like to specifically thank Dr. Lourenco for having a very impactful presence early on in my academic research roots.

I am deeply appreciative and thankful of all of the SiGe Devices and Circuits group members for their familial friendship to me. I want to specifically thank Adrian, Jeff, Zach, Sunil, Delli, Anup, and Patrick for their guidance when I am lost, help when measurements are not going well, help when I need more hands and I only have two, and always up for a beer after work to decompress.

I am forever indebted to my real close group of guys that I would label as closer than brothers: Squires, Asa, Spencer, John, and Blake. You all have walked with me through the toughest parts of my life and have loved me well and encourage me daily as long as it is called today.

Finally, I would like to thank my father Nikolay, my mother Lucy, my sister Melanie, and my stepdad Joe for their love and support and most importantly trying to understand what it means for their son to be an academic!

I love you all and I honestly could not have done any of this work without you and the many others in my life that are not listed here.

## TABLE OF CONTENTS

<b>Acknowledgments</b> . . . . .	v
<b>List of Tables</b> . . . . .	ix
<b>List of Figures</b> . . . . .	x
<b>List of Acronyms</b> . . . . .	xiii
<b>Chapter 1: Introduction To Radiation Effects</b> . . . . .	1
1.1 Space Radiation Environment . . . . .	1
1.1.1 Galactic Cosmic Rays . . . . .	1
1.1.2 Solar Energetic Particles . . . . .	3
1.1.3 Trapped Charge on Magnetically Active Planets . . . . .	4
1.2 The Radiation Effects in Electronics . . . . .	6
1.2.1 Overview of Single-Event Effects . . . . .	8
1.2.2 Overview of Total-Ionizing Dose . . . . .	10
1.3 Summary . . . . .	12
<b>Chapter 2: Introduction to SiGe Technology</b> . . . . .	13
2.1 Brief Theory of Operation . . . . .	13
2.2 Niche in Space Applications . . . . .	16

2.2.1	Radiation Resilience and Vulnerability . . . . .	17
2.2.2	Low Temperature Operation . . . . .	20
2.3	Summary . . . . .	21
<b>Chapter 3: TID Damage Effects on SiGe HBTs Across Temperature . . . . .</b>		<b>23</b>
3.1	Introduction . . . . .	23
3.2	Experimental Samples . . . . .	24
3.2.1	Silicon Germanium Technology . . . . .	24
3.2.2	Device Samples . . . . .	25
3.2.3	Low Noise Amplifier . . . . .	25
3.3	Measurement Setup . . . . .	27
3.3.1	System Configuration . . . . .	27
3.3.2	Device Measurements . . . . .	31
3.3.3	LNA Measurements . . . . .	32
3.3.4	In-Situ Measurement Methodology . . . . .	32
3.4	Device Measurement Results . . . . .	33
3.4.1	TID Damage in SiGe HBT At Room Temperature . . . . .	33
3.4.2	TID Damage Measured Across Temperature . . . . .	34
3.4.3	TID Damage When Radiated at Different Temperatures . . . . .	37
3.5	LNA Measurement Results . . . . .	40
3.5.1	TID Effects on LNA Gain . . . . .	40
3.5.2	TID Effects on LNA Noise Figure . . . . .	42
3.6	Summary and Future Work . . . . .	44

<b>Chapter 4: SET Trends in SiGe HBTs Across Temperature</b>	45
4.1 Introduction	45
4.2 Single Device SETs	45
4.2.1 Simulation Setup	45
4.2.2 Device Transient Results	47
4.3 Circuit-Level SETs	49
4.3.1 Circuit Selection	49
4.3.2 LNA Circuit Transient Results	51
4.4 Discussion	58
4.5 Summary and Future Work	59
<b>Chapter 5: Conclusion</b>	61
5.1 Contributions	61
5.2 Future Work	61
<b>References</b>	67

## LIST OF TABLES

1.1	Characteristics of galactic cosmic rays (GCRs). (After [1] and [4]) . . . . .	2
1.2	Characteristics of CMEs. (After [1]) . . . . .	4
1.3	Particle Composition in Radiation Belts. (After [1]) . . . . .	6
3.1	GlobalFoundries 9HP Specifications . . . . .	24
3.2	Bill-of-Materials . . . . .	28

## LIST OF FIGURES

1.1	The abundance of heavy ions in our solar system. (After [1] and [3]) . . . .	2
1.2	Side-by-side comparison of CME and solar flare. (Image courtesy: NASA and ESA.) . . . . .	3
1.3	A snapshot of the Earth's magnetosphere deflecting and trapping radiation that is ejected from the sun. For clarity the solar flare and the CME are labeled while the smaller text is from the original image. (Image courtesy: NASA, ESA, SOHO, LASCO, EIT) . . . . .	5
1.4	Van Allen belts. (Image courtesy: Wikipedia) . . . . .	5
1.5	Proton and electron fluxes in the radiation belts. Units are in $\text{cm}^{-2}\text{s}^{-1}$ . (After [5]) . . . . .	6
1.6	Saturn's radiation belts. The inset is zoomed to the inner most belt. (After [6]) . . . . .	7
1.7	A categorized timeline of various SEEs observed in electronics. (After [12])	8
1.8	An illustration showing the creation of free electrons and holes as a heavy ion passes through the semiconductor material. (After [13]) . . . . .	9
1.9	An example of an SET measured at a bipolar's collector terminal after a 400-MeV Ar ion passed through the device. Note that the SET's features are labeled accordingly. (After [14]) . . . . .	10
1.10	An illustration showing the process by which TID damage appears in semiconductor devices. (After [15]) . . . . .	11
2.1	SiGe HBT vertical structure with a diagram showing the Ge addition and the base doping profile (After [18]) . . . . .	14

2.2	Band diagram of a SiGe HBT showing the drift field in the base of the device which allows for assisted electron transport from the emitter to the collector of the device. (After [18]) . . . . .	15
2.3	A comparison between the Gummel curve of a silicon BJT (dashed) and a SiGe HBT (solid). With all parameters being equal except for the presence of Ge, the SiGe HBT realizes a much higher current gain. (After [18]) . . .	16
2.4	SiGe HBT cross-section showing the affected parts of the EB spacer and the STI. . . . .	18
2.5	Gummel curve of a SiGe HBT showing the 2kT slope on the base current. 1 kT and 2 kT lines are added to guide the eye. (After [22]) . . . . .	18
2.6	Current gain and transconductance of SiGe HBT across temperature. (After [29]) . . . . .	21
2.7	Gummel curves of a SiGe HBT across temperature. Note that the current gain is $I_c / I_b$ . (After [30]) . . . . .	22
3.1	Schematic of the LNA under test. . . . .	26
3.2	System diagram for the measurement configuration. . . . .	28
3.3	Exploded view of PCB (top), aluminum interposer (middle), and CryoTiger cold plate (bottom). . . . .	29
3.4	Real photo of the PCB mounted to the aluminum interposer with DUTs wirebonded to the PCB. . . . .	30
3.5	PCB construction viewed through CryoTiger radiation window. Internal RF cables used to connect to vacuum chamber port. Ribbon cable for DC connection. . . . .	30
3.6	Custom designed switch box when viewed from the (a) side and (b) top. . .	31
3.7	Comparison of forward and inverse mode damage. (a) Damage accumulation due to traps in the EB-spacer. (b) Damage accumulation due to traps in the STI. . . . .	35
3.8	Comparison of (a) forward and (b) inverse Gummel characteristics over temperature. The inverse Gummel shows more when damage measured at 300 K, but at 120 K almost all of the damage is hidden. . . . .	36

3.9	Comparison of apparent damage at different temperatures showing less apparent damage at low temperature. . . . .	37
3.10	Comparison of (a) forward and (b) inverse Gummel characteristics when irradiated at different temperatures. . . . .	38
3.11	Charge yield at different temperatures and electric fields [31]. . . . .	39
3.12	Comparison of gain when irradiated at (a) 300 K vs (b) 120 K. . . . .	41
3.13	Comparison of noise figure when irradiated at (a) 300 K vs (b) 120 K. . . .	43
4.1	A comparison showing GF 9HP results from the PDK to the 3-D TCAD calibration used in this study. . . . .	46
4.2	An example of ion-strike simulation captured immediately after the strike has begun. (Courtesy Dr. N. Lourenco) . . . . .	47
4.3	Simulation results showing the transient induced in a SiGe HBT by a heavy ion with LET = 10 MeV-cm <sup>2</sup> /mg at 300 and 250 K. . . . .	48
4.4	The circuit schematic of the LNA for this study. (Courtesy Dr. I. Song) . . .	50
4.5	The three configurations for inverse-mode use in the LNA. (Courtesy Dr. I. Song) . . . . .	51
4.6	Comparison of simulation to measured transient at the output of the LNA with the FF configuration. . . . .	52
4.7	Output voltage of the LNA as Q1 is struck with LET = 10 MeV-cm <sup>2</sup> /mg for 300, 250, and 150 K. . . . .	53
4.8	Collector current of the CE device (Q1) as Q1 is struck with LET = 10 MeV-cm <sup>2</sup> /mg for 300, 250, and 150 K. . . . .	55
4.9	Output voltage of the LNA as Q1 is struck with LET = 10 MeV-cm <sup>2</sup> /mg for 300, 250, and 150 K with FF, IF, and II topologies. Note that all of the axis are on the same scale. . . . .	56
4.10	CE Collector current of the LNA as Q1 is struck with LET = 10 MeV-cm <sup>2</sup> /mg for 300, 250, and 150 K with FF, IF, and II topologies. Dashed gray lines and solid arrows are displayed as references for the reader to see relative magnitudes between the stacked plots. . . . .	57



## ACRONYMS

<b>BJT</b>	bipolar junction transistor
<b>CME</b>	coronal mass ejection
<b>CML</b>	current-mode logic
<b>CMOS</b>	complementary metal-oxide-semiconductor
<b>COTS</b>	commercial, off-the-shelf
<b>DD</b>	displacement damage
<b>DUT</b>	device-under-test
<b>EB spacer</b>	emitter-base spacer
<b>EHP</b>	electron-hole pair
<b>EM</b>	electromagnetic
<b>FET</b>	field-effect transistor
<b>GCR</b>	galactic cosmic ray
<b>HBT</b>	heterojunction bipolar transistor
<b>IIP<sub>3</sub></b>	third-order intermodulation intercept point
<b>JPL</b>	Jet Propulsion Laboratory
<b>LNA</b>	low-noise amplifier
<b>mm-W</b>	millimeter-wave
<b>NF</b>	noise figure
<b>P<sub>1dB</sub></b>	1-dB compression point
<b>PCB</b>	printed circuit board
<b>PDK</b>	process design kit
<b>RF</b>	radio frequency
<b>RHBD</b>	radiation-hardening-by-design

**SCR** space-charge region  
**SEE** single-event effect  
**SET** single-event transient  
**SiGe** silicon-germanium  
**SMU** source-measuring unit  
**SoC** system-on-chip  
**SP8T** single-pole 8-throw  
**STI** shallow-trench insulator  
**SWaP** size-weight-and-power  
**TID** total-ionizing dose

## SUMMARY

The objective of this research is to investigate the effect that low temperature has on the radiation effects on advanced silicon-germanium (SiGe) heterojunction bipolar transistor (HBT) for the application of deep-space exploration missions that are specifically classified as extreme low-temperature and highly radiation active environments, such as Jovian exploration missions. We designed a unique experimental testbed that enabled DC and RF measurements to be taken in situ at various temperature and radiation points. The experiment was conducted at the Jet Propulsion Laboratory (JPL) where low-temperature and radiation environments can be mimicked. We showed that while there is some radiation damage in base leakage current on the single transistor level, there is no observed damage due to total-ionizing dose (TID) in noise figure, linearity, or gain for a 2.4 GHz low-noise amplifier (LNA) that was irradiated at an ambient temperature of about 100 K up to 1 Mrad (Si). Furthermore, we confirmed the notion that radiation at lower temperatures yields less damage and showed why it is important to separate temperature-dependent performance with measurable radiation damage at different temperatures.

We also took a simulation approach to determine whether single-event transients (SETs) get worse as a result of the device being in low ambient temperatures. For a single standalone device, the results show that the transient gets larger in magnitude but shorter in duration. However, the circuit results show that the effects of an SET get worse in some cases with low temperatures such as in the context of LNAs, but can also get better in other cases such as current-mode logic (CML) D-flip-flops.

Chapter 1 presents an overview of the radiation climatology in space. It also goes into a little more detail about the different physical effects that radiation has in electronic devices.

Chapter 2 introduces the basic theory and operation of SiGe HBTs. It then goes into even more detail about the current state of understanding of how radiation specifically impacts SiGe HBTs. This chapter also includes a brief introduction on how low temperatures

affect the performance of SiGe HBTs.

Chapter 3 covers an experiment that was done to understand how low temperatures impact the TID response of a SiGe HBT. The experiment was further extended to incorporate an LNA to see if any of the circuit metrics get degraded with TID at low temperatures.

Chapter 4 covers a simulation study done to understand how low temperatures change the SET response of SiGe HBTs. The latter part of this chapter also includes an LNA simulation that incorporates an SET mitigation technique. Over-temperature trends are shown and explained.

Chapter 5 provides an overall conclusion to this thesis as well as future work that is suggested to continue this work.

# CHAPTER 1

## INTRODUCTION TO RADIATION EFFECTS

### 1.1 Space Radiation Environment

Space contains a myriad of highly energetic particles that zoom across our entire universe and can be found virtually anywhere. These particles originate from two major astronomical events: 1) cataclysmic interstellar events such as supernovae and star collisions, and 2) natural star decay, i.e. our sun burning. The phenomena of these highly-energetic particles moving through our universe is what is referred to as space radiation, or simply radiation for short. For a more complete view of space climatology in the context of radiation effects in electronics, the interested readers are referred to [1].

#### 1.1.1 Galactic Cosmic Rays

Supernovae and star collisions indubitably produce an extreme amount of energy. On an atomic level, the magnitude of the expelled energy is enough to ionize nearby atoms by stripping off their own electrons from their nuclei. This process can create ions as heavy as iron. But if there is an abundance of neutrons present (e.g., neutron star collision), then higher-order fusion can occur creating even heavier elements such platinum or gold. Regardless of the element, these particles are shot out from events like these to the extents of space with GeV and TeV energies. These particles are commonly referred to as galactic cosmic rays (GCRs). The abundance of GCRs in our own solar system is shown in Fig. 1.1. Note that there is a significant reduction in the abundance of GCRs that are heavier than iron since iron is the heaviest element fused inside of a star [2]. Also listed in Table 1.1 is a breakdown of the relative percentages of occurring GCRs where it can be seen that about 99% are protons and alpha particles.

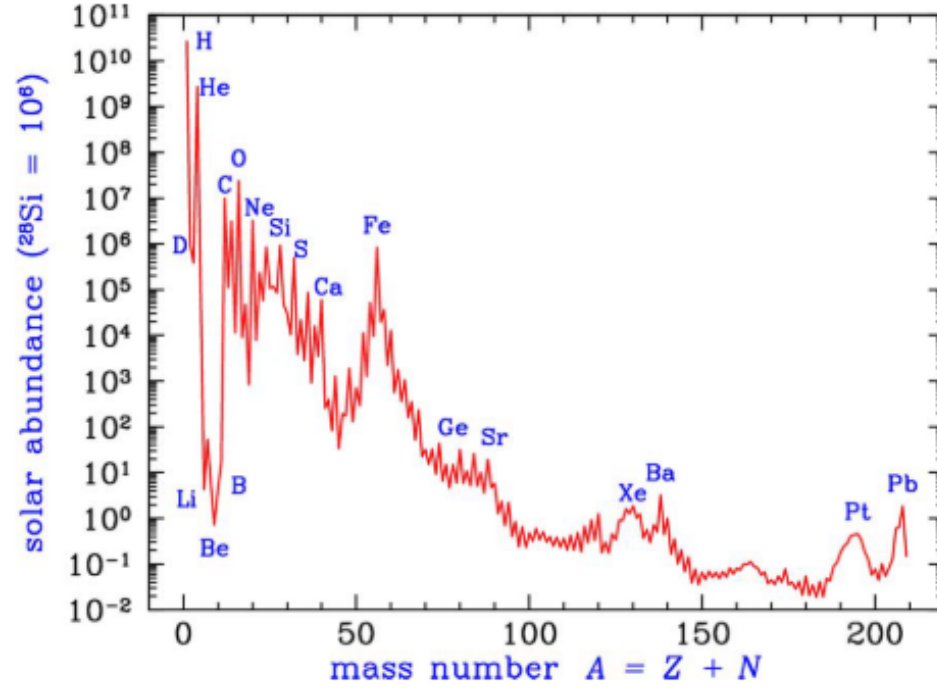


Figure 1.1: The abundance of heavy ions in our solar system. (After [1] and [3])

Table 1.1: Characteristics of GCRs. (After [1] and [4])

Hadron Composition	Energies	Flux
90% protons	Up to $\sim 10^{20}$ eV	1 to $10 \text{ cm}^{-2}\text{s}^{-1}$
9% alphas		
1% heavier ions		

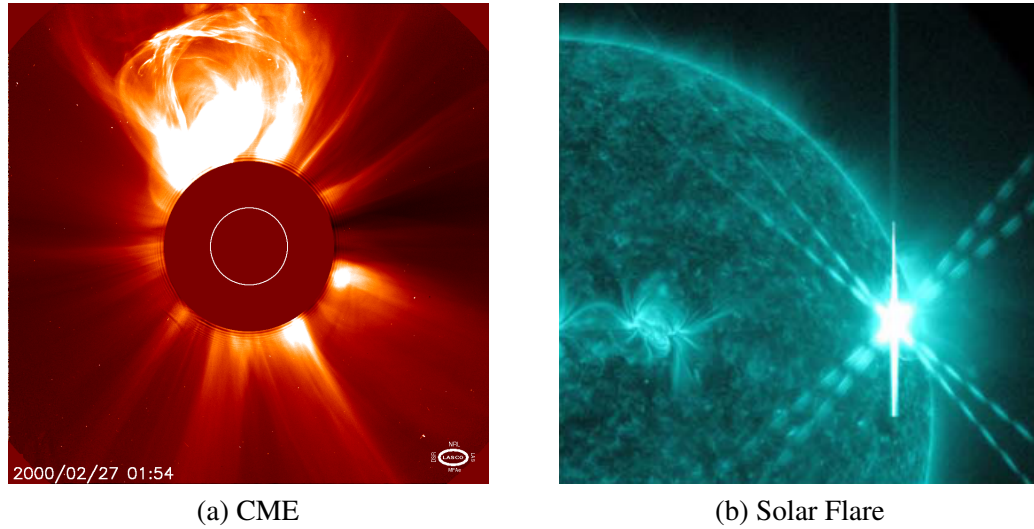


Figure 1.2: Side-by-side comparison of CME and solar flare. (Image courtesy: NASA and ESA.)

### 1.1.2 Solar Energetic Particles

Stars, like our sun, are very good at giving off a significant amount of energy. While this energy is one of the life-giving ingredients for our planet Earth in the form of light and heat, it is also one of the main producers of radiation in our solar system. On the surface of the sun, two main violent processes release energetic particles into the solar system: solar flares and coronal mass ejections (CMEs). Typically, CMEs are more of a threat to electronics from a radiation perspective because they eject a larger amount of mass with more energy from the sun than solar flares. Another key difference is that solar flares emit photons rather than particle mass, i.e. protons, and travel at the speed of light, which is why they appear to be brighter than CMEs. Fig. 1.2 shows a side-by-side comparison of a CME and a solar flare; note how much larger the CME is than the solar flare. Table 1.2 shows some of the characteristics that are associated with CMEs. Note that most of the mass that is ejected from the sun is comprised of protons. The solar flare characteristics are omitted since they do not eject a large amount of energetic particles.

Table 1.2: Characteristics of CMEs. (After [1])

Hadron Composition	Energies	Flux
96.4% protons	Up to $\sim 10^{10}$ eV	Up to $\sim 10^6 \text{ cm}^{-2}\text{s}^{-1}$
3.5% alphas		
0.1% heavier ions		

### 1.1.3 Trapped Charge on Magnetically Active Planets

Since GCRs and solar energetic particles are ionized, meaning they have one or more of their electrons stripped, they are influenced by magnetic fields according to Maxwell's equations. Planets that have a magnetosphere (created by the movement of electrically conductive fluids in their cores) can trap these charged particles in their atmosphere. Depending on the strength of the magnetosphere, there can be severe limitations in space missions that are set in these magnetospheres. Fig 1.3 shows an example of this relationship between the Earth and the sun where solar particles ejected by CMEs and the more constant solar wind, are being deflected and trapped by Earth's magnetosphere. The asymmetry of the magnetosphere is caused by the perturbation of the ionized solar particles which reorient the Earth's magnetic field lines. It is worth noting that without Earth's magnetosphere, the highly energetic solar particles would essentially annihilate all life on Earth.

A closer look at Earth's magnetosphere reveals that it has two primary magnetic shells as shown in Fig. 1.4: the inner zone and the outer zone. These belts, known as the Van Allen belts, are the locations where most of the space radiation gets trapped around Earth. The inner zone is mostly made up of protons and originates from several collision processes started with GCR collisions with Earth's atmosphere. The outer belt mainly consists of captured electrons and a few protons that are ejected from the sun [5]. Fig. 1.5 shows the fluxes for trapped protons and electrons as a function of Earth radii. Table. 1.3 shows some of the characteristic energies and fluxes of the trapped particles. It is important to note that these radiation belts should be taken into account when planning any type of mission that would stay or pass through the belts.



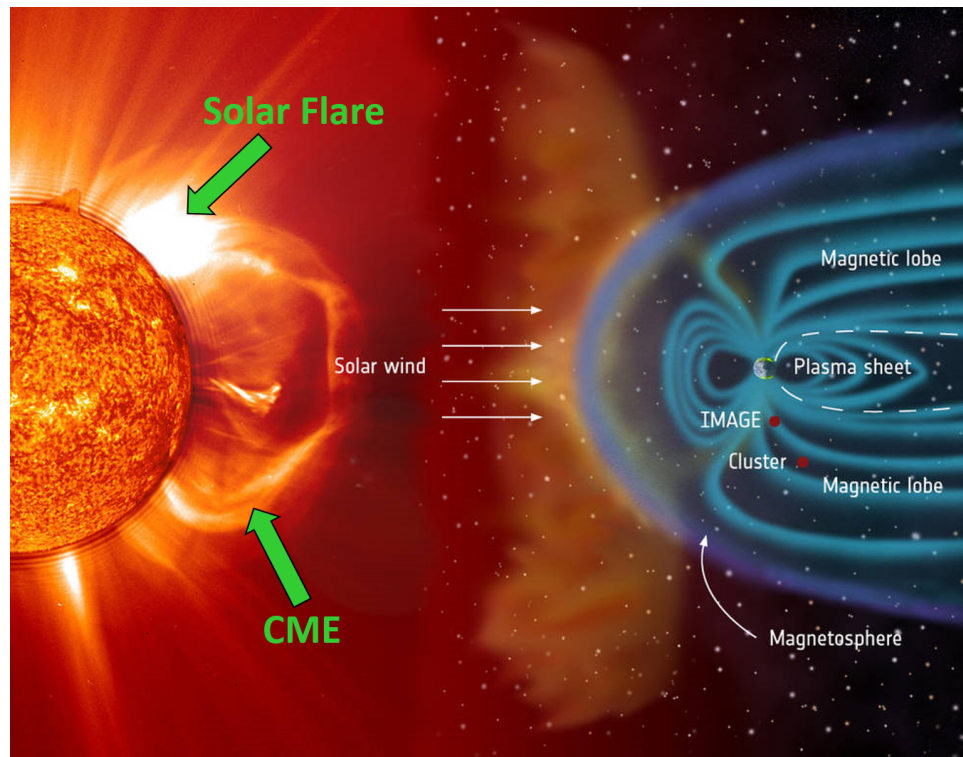


Figure 1.3: A snapshot of the Earth's magnetosphere deflecting and trapping radiation that is ejected from the sun. For clarity the solar flare and the CME are labeled while the smaller text is from the original image. (Image courtesy: NASA, ESA, SOHO, LASCO, EIT)

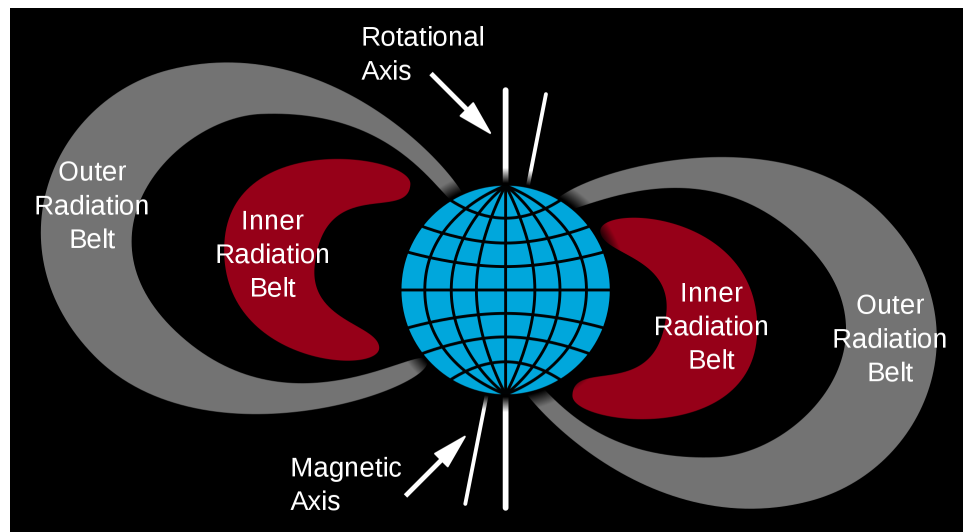


Figure 1.4: Van Allen belts. (Image courtesy: Wikipedia)

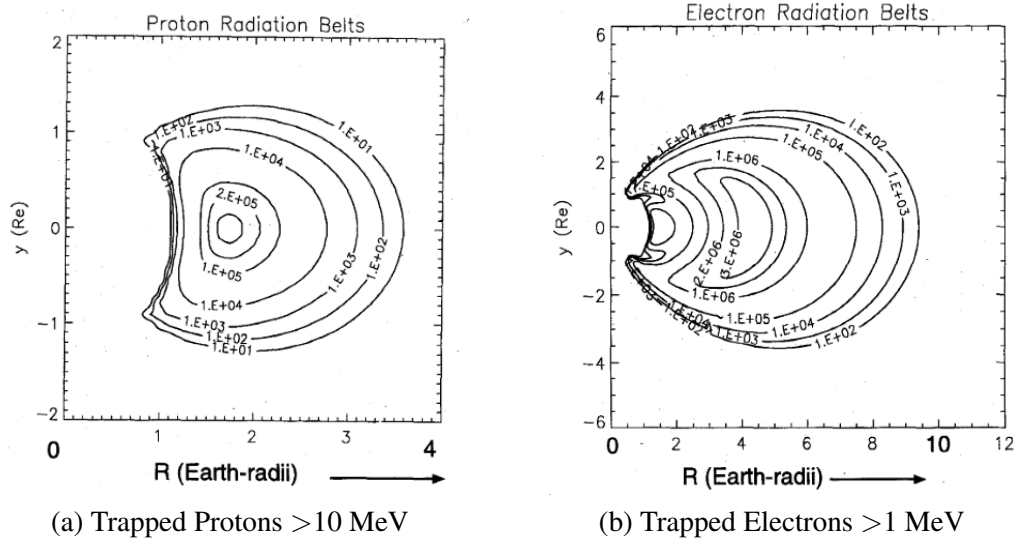


Figure 1.5: Proton and electron fluxes in the radiation belts. Units are in  $\text{cm}^{-2}\text{s}^{-1}$ . (After [5])

Table 1.3: Particle Composition in Radiation Belts. (After [1])

	Radiation Belt	Energies	Fluxes ( $\text{cm}^{-2}\text{s}^{-1}$ )
Trapped Protons	Inner	Up To 1 GeV	Up To $10^5$
Trapped Electrons	Inner	Up To 5 MeV	uncertain
	Outer	Up To 10 MeV	Up To $10^6$

Jupiter and Saturn also have magnetospheres that trap ionized particles in their own radiation belts. Saturn's radiation belts, both of which are shown in Fig. 1.6, are weaker due to the strong absorption of its rings and moons that perturb the free charges [6] [7]. However, Jupiter's magnetosphere and radiation belts are much stronger (the strongest in the solar system) [8]. This means that Jupiter can capture much higher energies and densities of ions in its radiation belts. Up to one thousand or one million times the energies and fluxes of protons and electrons have been predicted to be in the Jovian radiation belts [9].

## 1.2 The Radiation Effects in Electronics

It is important to understand the radiation climatology because radiation can heavily interfere with the on-board electronics of a spacecraft and can even cause mission failure if

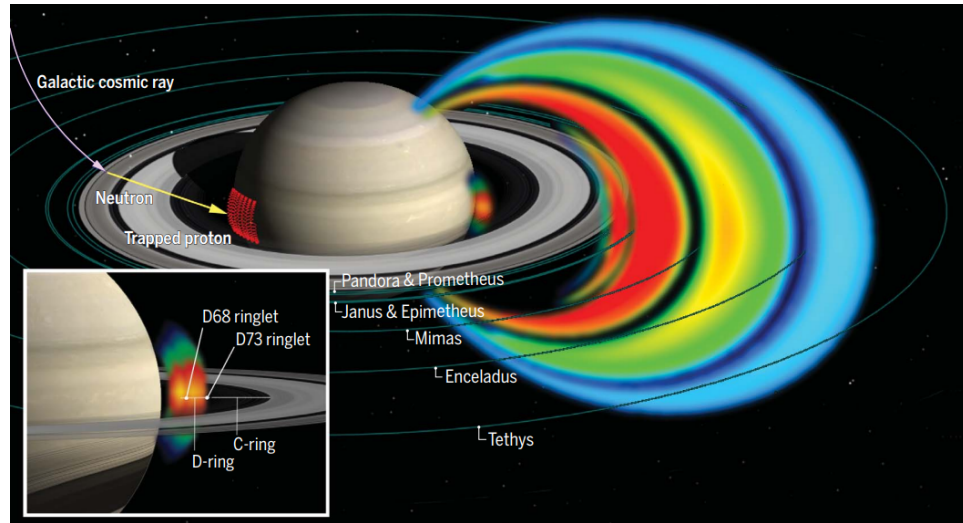


Figure 1.6: Saturn's radiation belts. The inset is zoomed to the inner most belt. (After [6])

not addressed properly. Radiation is also a difficult thing to shield against since it typically involves using thicker and more dense metals adding to the overall weight and cost of the spacecraft. Furthermore, metal shielding can help against some of the smaller particles like electrons or protons, but really high-energy GCRs can still penetrate the shield. Thus, radiation effects in electronics is still a widely researched topic. The goal with a lot of the on-going research is to understand how the various particles in space interact with semiconductor devices, the types of physical and electrical effects induced by these energetic particles, and most importantly, how engineers and designers can use this information to make the next generation of electronics more resilient to radiation.

Radiation effects in electronics can generally be categorized in three different buckets: single-event effects (SEEs), total ionizing dose (TID), and displacement damage (DD). However, in this thesis only TID effects and SEEs will be looked at in depth. For more information about DD effects, the reader is referred to [10, 11] for a comprehensive review of this topic.

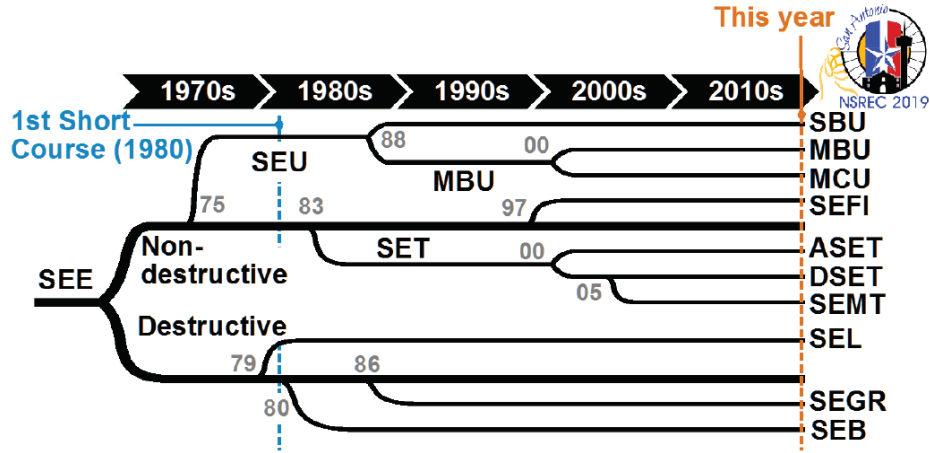


Figure 1.7: A categorized timeline of various SEEs observed in electronics. (After [12])

### 1.2.1 Overview of Single-Event Effects

SEEs have to do with a perturbation of a device or system caused by a single particle (e.g., heavy ion) passing through the semiconductor and transferring its energy. This process can either be destructive meaning that the device or system is permanently damaged and non-recoverable, or non-destructive meaning that the perturbation can cause errors in functionality but only for a limited time whereafter the device or system can go back to functioning in its normal conditions. Whether or not the effect is destructive or non-destructive is determined by the crystal/material structure, the device type, and the damage thresholds for the device in question. A categorized timeline of the various SEEs observed in electronics is shown in Fig. 1.7. For this thesis, it is the single-event transient (SET) that will be the topic of interest since it is the most important for SiGe heterojunction bipolar transistors (HBTs). For a more in-depth look at SEEs in electronics, [12] is a good fundamental source that explains these effects.

As a heavy ion enters a semiconductor crystal it deposits its energy into the system. Bound electrons and holes along the path of the heavy ion absorb that energy and become free carriers in the semiconductor as illustrated in Fig.1.8. Both drift and diffusion processes are responsible for the movement of the newly generated free carriers. A heavy

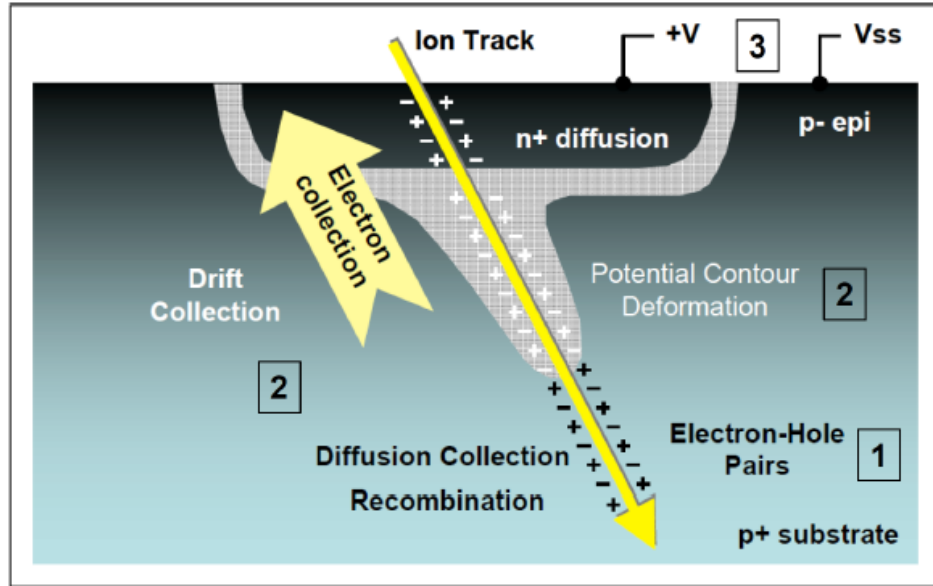


Figure 1.8: An illustration showing the creation of free electrons and holes as a heavy ion passes through the semiconductor material. (After [13])

ion can create peak carrier concentrations in excess of  $10^{20}\text{cm}^{-3}$  in silicon so the diffusion process will move carriers away from the ion strike, where these carriers are densely packed, and possibly towards an active device. The drift process only occurs if there is an electric field present. The space-charge region (SCR) in an active semiconductor device intrinsically sustains an electric field, so if the free carriers enter a device's SCR they will experience its electric field and get pushed in the direction of the field. For example, this can be seen in the illustration in Fig. 1.8 when electrons get pulled up towards the surface due to the drift field that is present. It is possible for a fraction of the generated carriers to end up collected by the terminals of the device as an extra current spike or a transient (i.e., an SET). An example of what this SET might look like is shown in Fig. 1.9 with all of its features colored and labeled. Note that if the current produced from an ion strike exceeds any damage threshold of a device, then the SEE becomes destructive and the device will fail.

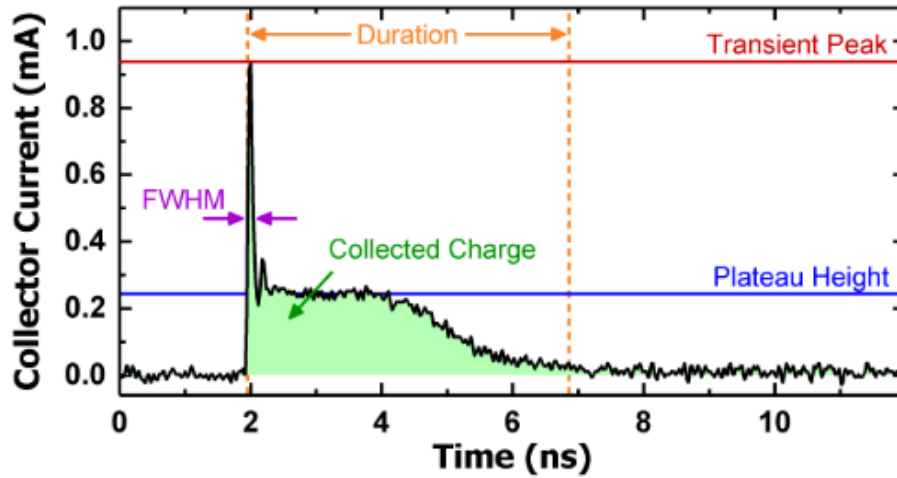


Figure 1.9: An example of an SET measured at a bipolar's collector terminal after a 400-MeV Ar ion passed through the device. Note that the SET's features are labeled accordingly. (After [14])

### 1.2.2 Overview of Total-Ionizing Dose

TID on the other hand has a cumulative effect rather than a singular effect even though the basis is the same, namely an impinging particle producing free electrons and holes in the system. However, in the TID case, the carriers that produce the damage are the ones generated within the insulating materials of the device (e.g., silicon-oxides). An illustration showing how the damage gets formed is shown in Fig. 1.10. First, the impinging particle creates an electron-hole pair (EHP) inside the oxide material. Then, if there is an electric field present across the oxide, such as that of the gate of a field-effect transistor (FET), it splits the EHP spatially with the electron and hole going in opposite directions. The electron's mobility in an oxide is much greater than the hole so it gets flushed out of the oxide while the hole "hops" towards the interface where the oxide ends. There are two possibilities for the hole to undergo: 1) the hole gets trapped in the oxide due to a defect, making the oxide charged, or 2) the hole makes it to the interface where it interacts with a hydrogen atom, frees it, and leaves behind an  $\text{SiO}_2$  dangling bond i.e., an interface trap. Both of these results can negatively impact the device especially if the oxide in question

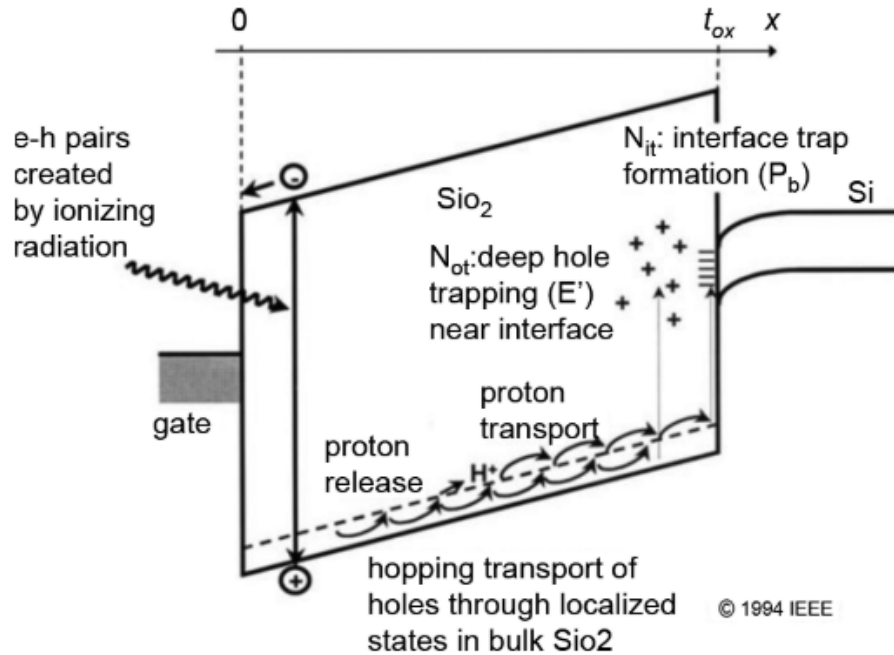


Figure 1.10: An illustration showing the process by which TID damage appears in semiconductor devices. (After [15])

is next to an active part of the device. However, note that in contrast to an SEE, a single trapped hole or an interface trap will be negligible as there is no perfect interface or perfect crystal. The non-negligible damage begins to affect the device after many of these trapped holes or interface traps get generated, which is why this is a cumulative effect.

This is most easily understood with FETs devices as the gate is an important oxide for device functionality. For example, if an n-type FET is subject to a large fluence of ionizing radiation, based on the process described earlier, its gate oxide will get positively charged which will reduce its effective threshold voltage. If enough ionizing radiation goes through the gate, it could eventually charge it so much that the nFET will no longer be able to turn off and essentially be deemed useless. For a more in-depth and detailed analysis of this phenomenon, the reader is referred to [16, 17].

### 1.3 Summary

Radiation in the space environment is best understood in the context of a “climate” since it is constantly changing but overall exists in rhythms and patterns depending on your specific location. For example, near-sun missions should expect highly dense proton clouds emitted from CMEs, while missions that go beyond our solar system which require the spacecraft to spend much of its time in empty space should expect a larger flux of GCRs as there is no protection or influence from any other celestial bodies. So it is always important when talking about radiation effects in the context of missions to space to understand what types of particles and how many of them each mission will see. Once that is well understood, careful consideration must be given to the types of electronics that the spacecraft will have on board. Engineers must take extra precautions not to use electronics that might permanently be damaged by radiation, which can cause a severe loss of data, or worse, lose control of the spacecraft altogether. While it is not the main topic of this thesis, it is worth noting that some mitigation strategies exist to make electronics more robust, but mitigation most often comes with overhead, extra costs, extra space, or a decrease in performance of the system. (One of these mitigation strategies will be briefly explored in Chapter 4.) In summary, radiation is abundant in space and its effects in electronics is a major concern for the success of any mission.



## **CHAPTER 2**

### **INTRODUCTION TO SIGE TECHNOLOGY**

This chapter provides a brief introduction to SiGe HBT technology in the context of basic operation and its niche in space applications. The interested reader looking for a deeper understanding of the technology's history, fundamental physics and derivations, and the importance in today's commercial and space markets is referred to [18].

#### **2.1 Brief Theory of Operation**

SiGe HBTs are bandgap-engineered bipolar devices aimed to improve the performance of RF circuits that require lower noise performance and much higher gain in the larger GHz frequency ranges than its complementary metal-oxide-semiconductor (CMOS) cousin. The lure of SiGe HBTs is that they are fabricated in mature silicon processes on the same substrate as CMOS, thereby reducing the cost to fabricate and increasing the availability for the larger market compared to the exotic III-V semiconductor technologies. SiGe HBTs are vertical transport devices which means that foundry lithography limits do not affect its performance to first order. This is a huge advantage in cost-performance since one can utilize 200 GHz SiGe HBT devices in a 120-nm process [19]. It would be incorrect to claim that SiGe HBTs are “better” than silicon CMOS. However, it is important to understand that at a fixed lithographic node, SiGe HBTs can provide an advantage in speed and noise performance to be used alongside CMOS. In general, with a SiGe BiCMOS platform, one can use the advantage of CMOS digital design with the advantage of SiGe analog or RF design to produce a low-cost, monolithic system-on-chip (SoC).

SiGe technology utilizes bandgap engineering to alter the bandgap of a typical silicon bipolar's base region by introducing germanium into the device. Fig. 2.1 illustrates the general structure of the SiGe HBT, on the left, with a diagram of where the Ge is placed in

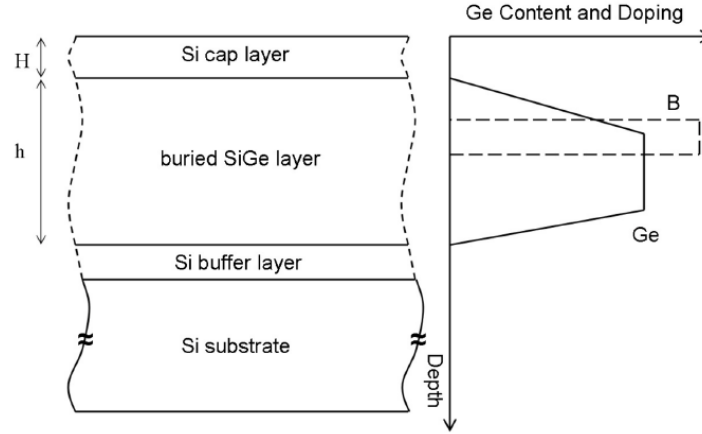


Figure 2.1: SiGe HBT vertical structure with a diagram showing the Ge addition and the base doping profile (After [18])

the device on the right. The more narrow bandgap of Ge in the base produces an intrinsic electric field that assists electron transport from the emitter of the device to the collector. A generic band diagram of a typical SiGe HBT is shown in Fig. 2.2. Note that the introduction of a graded Ge profile (i.e. not constant) creates two major advantages: 1) it gives rise to a built-in drift field across the base that assists electron transport, and 2) it decreases the emitter-base energy barrier of the conduction band.

When the conduction band energy barrier between the emitter and base is reduced, it allows for more electrons to be injected from the emitter to the base than in a silicon bipolar junction transistor (BJT). To illustrate this effect, a controlled experiment was conducted between a silicon BJT and a SiGe HBT and their respective current-voltage transfer characteristics, known as the Gummel, are shown in Fig. 2.3. With the presence of Ge being the only parameter changed, the SiGe HBT exhibits a larger current gain than a silicon BJT. The main advantage of the reduction in the emitter-base barrier, however, is in the fact that from an engineering perspective, one can tune the current gain of the SiGe HBT simply by controlling how much Ge is present at the emitter-base junction. In contrast, the only tuning knob of a Si BJT on its current gain is the emitter to base doping ratio. In other words, with the presence of Ge, one can decouple the current gain of the bipolar from the

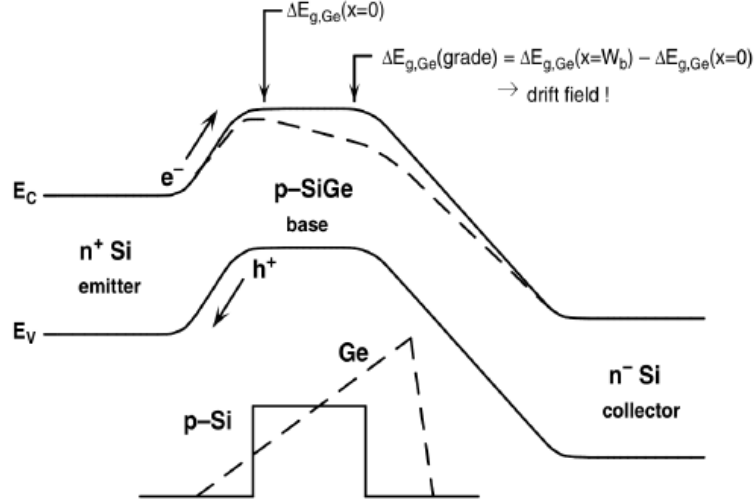


Figure 2.2: Band diagram of a SiGe HBT showing the drift field in the base of the device which allows for assisted electron transport from the emitter to the collector of the device. (After [18])

emitter to base doping ratios. This in turn enables the SiGe HBT to have large current gain while simultaneously having higher base doping than what was originally possible with the Si BJT.

Higher base doping has many advantages, but one of the main advantages is that the sheet resistance of the base decreases with increased doping. From a speed perspective this variable increases the maximum oscillation frequency  $f_{MAX}$  which is the maximum frequency of the transistor to realize power gain. The equation for  $f_{MAX}$  is

$$f_{MAX} = \sqrt{\frac{f_T}{8\pi R_B C_{CB}}} \quad (2.1)$$

where  $R_B$  is the base resistance,  $C_{CB}$  is the collector-base capacitance, and  $f_T$  is the maximum frequency that the transistor has current gain (also known as cut-off frequency). The maximum  $f_T$  achieved in a SiGe HBT is highly dependent on the time an electron takes to go from the emitter, through the base, and into the collector. The built-in drift field created by the graded Ge assists the electron as it goes through the base, which in turn increases

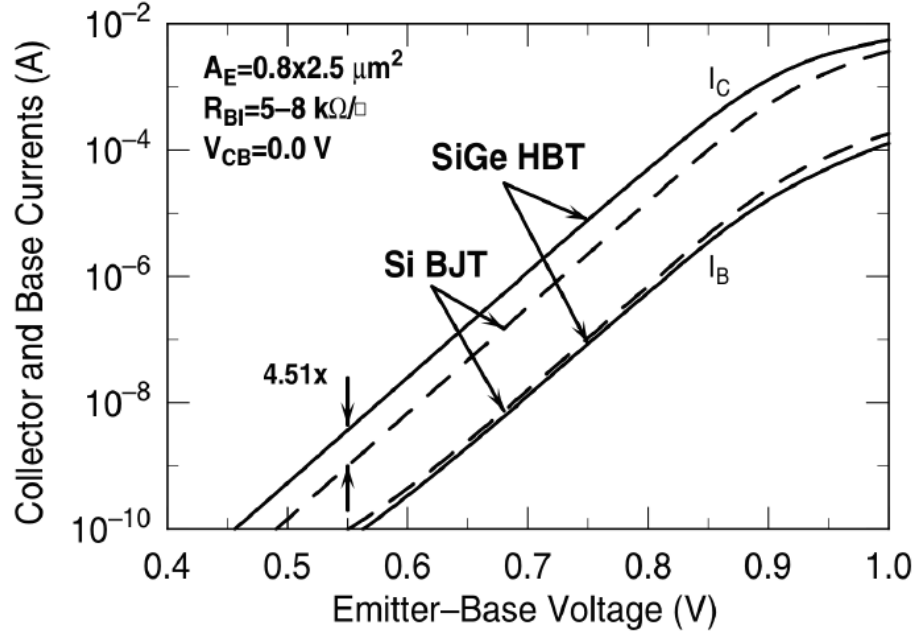


Figure 2.3: A comparison between the Gummel curve of a silicon BJT (dashed) and a SiGe HBT (solid). With all parameters being equal except for the presence of Ge, the SiGe HBT realizes a much higher current gain. (After [18])

the maximum  $f_T$ . The parameters  $f_T$  and  $f_{MAX}$  are called figures of merit and are used by foundries and researchers to benchmark their technology. Typically for high-performance platforms, designers want as much  $f_T$  and  $f_{MAX}$  as they can get.

While there are a lot more physics and interesting studies done with this device over the past 30 years, this brief introduction is all that is needed to understand the contents of this thesis.

## 2.2 Niche in Space Applications

One of the most promising applications for SiGe technology are electronics that must operate in extreme environments. Extreme environments can include extremely wide temperature variations, intense radiation, extreme pressures, and many more. The space environment that was described in Chapter 1 is considered an extreme environment due to the potential of high doses of radiation and really wide temperature swings depending on the space mission. There are two review papers [20, 21] that go in depth with many experi-

ments and analyses specifically with the use of SiGe technology for extreme environments. In this section, an overview will be given that touches on radiation effects in SiGe and its low-temperature operation. As those two review articles suggest, there have been plenty of studies and experiments conducted with SiGe HBTs in terms of their radiation response (TID and SEE) and their low-temperature performance. However, there have been very few studies done that provide information on how low temperatures affect the TID and SEE response. The exploration of this synergistic effect is the basis of this thesis.

### 2.2.1 Radiation Resilience and Vulnerability

#### *Total Ionizing Dose in SiGe HBTs*

As mentioned earlier in Chapter 1, TID damage mostly affects electronic devices when there are dielectric layers present around where carrier transport is happening. This is because TID charges up the dielectric layer and creates defects along the semiconductor-dielectric interface. In a SiGe HBT there are two oxides present in the structure that could pose a threat if the device accumulates total dose: the emitter-base spacer (EB spacer) and the shallow-trench insulator (STI). An overview of the SiGe HBT cross-sectional structure along with the oxides in question are shown in Fig. 2.4. Due to Shockley-Reed-Hall (SRH) recombination, the traps on the interfaces that are within the SCR of the HBT are going to give rise to recombination current (also referred to as leakage current). The recombination current has an indicative  $2kT$  slope in the Gummel curve of the transistor as shown in Fig. 2.5 where  $k$  is Boltzmann's constant and  $T$  is the temperature. At 300 K, this slope equates to roughly 120 mV/decade of current. A pristine, non-damaged HBT will only have a  $1kT$  slope which equates to about 60 mV/decade of current. This is clearly seen in Fig. 2.5 where the radiated measurements show an increase in base current at low  $V_{BE}$ . The radiation damage in the EB spacer only increases the base current which in turn decreases the current gain of the transistor.

However, note that at higher base-emitter voltages (around 0.8 V), the radiation-induced

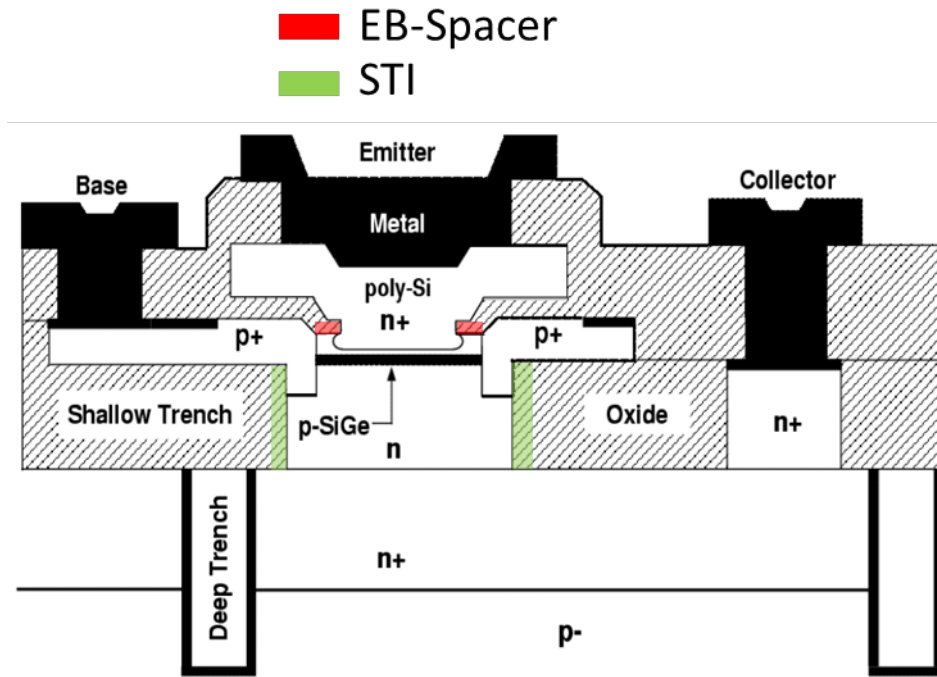


Figure 2.4: SiGe HBT cross-section showing the affected parts of the EB spacer and the STI.

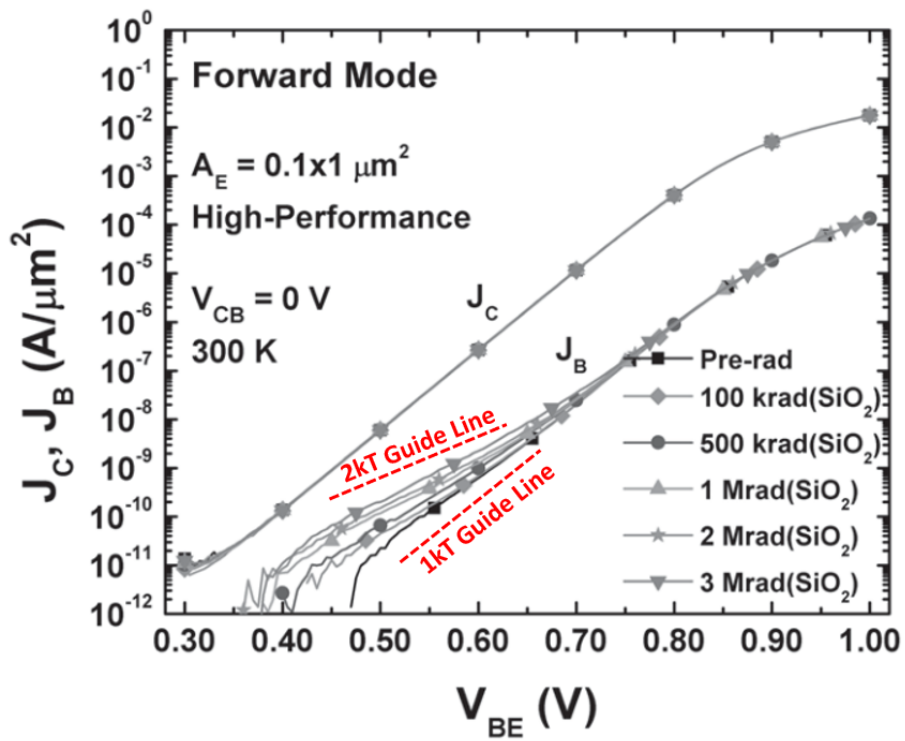


Figure 2.5: Gummel curve of a SiGe HBT showing the 2kT slope on the base current. 1 kT and 2 kT lines are added to guide the eye. (After [22])

$2kT$  current falls below the HBT's regular  $1kT$  current and the HBT looks like it has not been electrically damaged. The current gain goes back to what it would have been pre-rad. Keep in mind that these HBTs are typically biased at  $V_{BE} > 0.8$  V where they perform at peak  $f_T$  and  $f_{MAX}$ . This is why it is typically said that SiGe HBTs are “multi-Mrad hard” meaning that they can withstand a large amount of dose and still perform just fine. As a reference, a satellite in geosynchronous orbit will accumulate around 100 krad(SiO<sub>2</sub>) of dose over 10 years [23]. Clearly SiGe HBTs can handle this type of an environment from a TID perspective.

The STI on the other hand does not play a significant role when the transistor is working in the forward mode. This is because the base-collector junction is reverse biased so there is no SRH recombination current that goes through that junction. However, when the HBT is operated in inverse mode, the base-collector junction becomes the forward-biased junction while the base-emitter junction becomes the reverse-biased junction. So in inverse mode, the damaged STI by TID is the cause for the  $2kT$  recombination current.

Overall, it can be said that whether in inverse mode or forward mode, TID poses very little threat to the functionality of a SiGe HBT at room temperature.

#### *Single-Event Effects in SiGe HBTs*

On the other hand, SEEs have been shown to be a serious concern for SiGe HBTs. This is because when a heavy ion strikes any device, the magnitude of the transient that will show up at the terminals of the device is heavily dependent on how fast the device can respond and collect the generated EHPs. Since the SiGe HBT is shown to have high gain at relatively high frequencies, it is no surprise that as the SiGe HBT gets faster and better with technology scaling and maturity (meaning the fabrication techniques are allowing the HBT to improve in performance), the SET response will get worse [24].

An important thing to note is that single events for SiGe HBTs are non-destructive which essentially means that, to date, no permanent damage has been observed in SiGe

HBTs that is directly due to a heavy-ion strike. So the biggest concern with heavy ions striking SiGe HBTs is that the generated transients can alter data stored on the device and thus cause bit-errors, or it can perturb a control signal which can cause system failure [25, 26, 27].

In general, it can be said that SiGe HBTs are highly vulnerable to SEEs, which is one of the reasons why mitigation strategies to suppress SEEs are still researched today.

### 2.2.2 Low Temperature Operation

Electronics operating at extremely low temperatures have been studied over the past several decades for many reasons. Some specific applications include quantum computing read-out circuitry, deep-space electronics, single-photon detectors, and many more. SiGe technology has been a huge contender in this field since its performance improves at lower temperatures. In 2014, a commercially available SiGe HBT was measured at record speeds of 800 GHz  $f_{MAX}$  at 4.3 K [28]. One of the main reasons why the high performance SiGe HBTs can operate at low temperatures is because the bandgap-engineered Ge decouples the doping profile from the gain and speed of the device. In other words, the SiGe HBT can have relatively high doping concentrations in the emitter, base, and collector (unlike its silicon BJT counterpart) with concentrations above the Mott transition. What this means is that carrier freeze-out is insignificant, and the device will still function and actually experience an increase in its current gain as shown in Fig. 2.6. One of the benefits for electronics in low-temperature environments is that the thermal energy of the lattice decreases and carriers scatter less often from the crystal. This effect increases the mobilities of the carriers [29] and reduces the thermal noise of the system: clearly all good things.

Another study that was aimed specifically for the potential of SiGe HBTs to be used as read-out circuitry for quantum computing was conducted in 2017 [30]. It was found that SiGe HBTs can indeed function at temperatures as low as 70 mK. While more research needs to be done to understand some of the device physics at those low temperatures, the



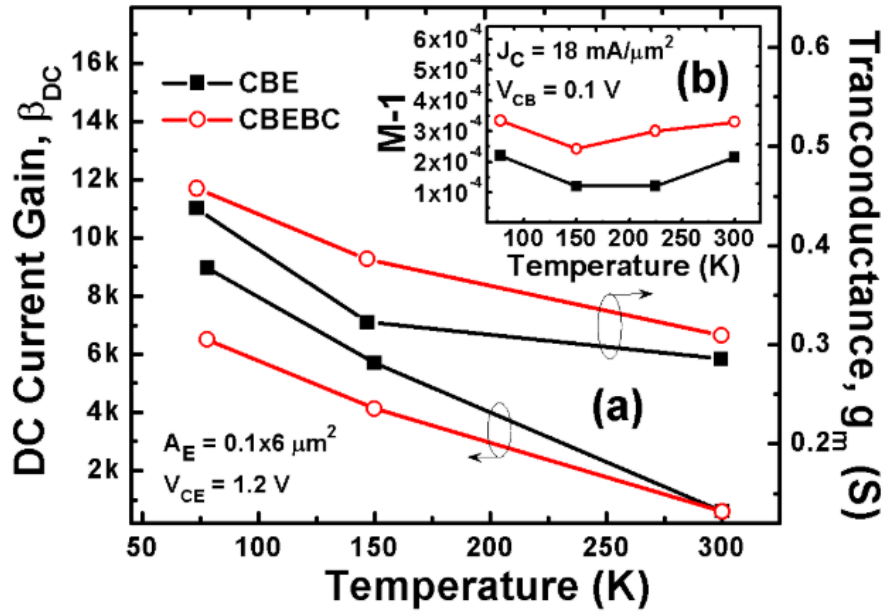


Figure 2.6: Current gain and transconductance of SiGe HBT across temperature. (After [29])

SiGe HBT nonetheless exhibits an appreciable gain as shown in the Gummel characteristics in Fig. 2.7 (note that the current gain is simply  $I_c / I_b$  in this figure).

The improved operation of SiGe HBTs at low temperatures is important in the space electronics context because many of the missions that are aimed at investigating planets and objects away from the sun (e.g. Jupiter, Pluto, Europa) have ambient temperatures as low as 50 K. Therefore, from a low-temperature perspective, SiGe HBTs have shown high resiliency and a large potential to be used for deep space applications.

### 2.3 Summary

The SiGe HBT is a very complicated device in terms of its physics and operation, though some of the basic physics and operations (that barely scratch the surface) were presented in the beginning of this chapter to provide context for the reader. It was then shown that SiGe HBTs are highly resilient to TID damage, but very vulnerable to SEEs. At low temperatures, the SiGe HBT increases its performance in terms of gain, speed, and noise.

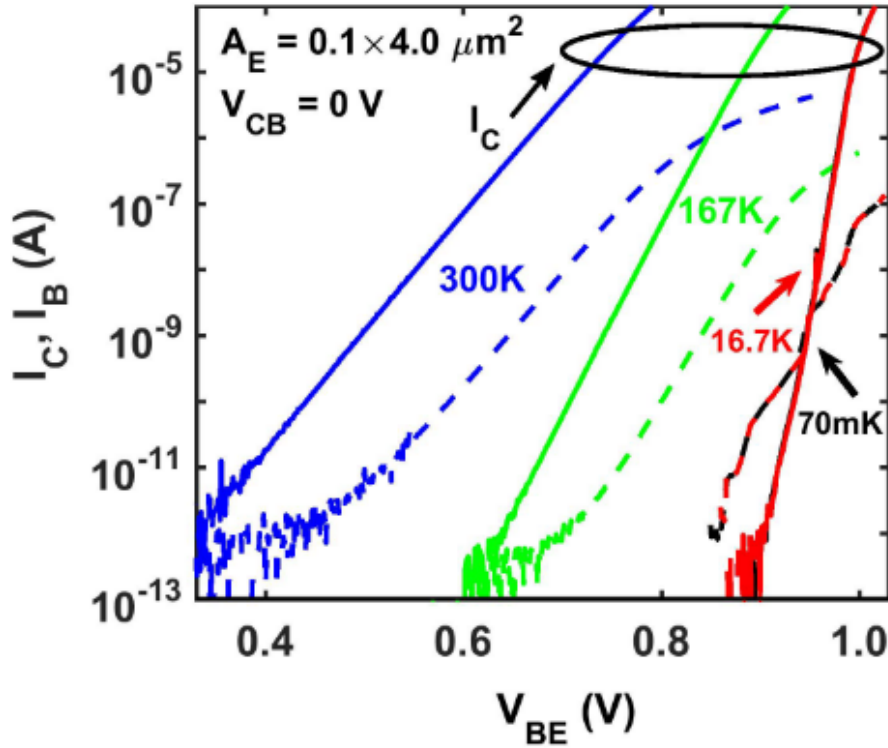


Figure 2.7: Gummel curves of a SiGe HBT across temperature. Note that the current gain is  $I_C / I_B$ . (After [30])

However, the question still remains: if SiGe HBTs show an improved performance at low temperatures, then how does the device respond to TID damage and heavy-ion strikes? With increased performance, will the TID damage be more significant? Will SETs get worse? In the following chapters, two different studies will be presented in an attempt to answer these questions.

## CHAPTER 3

### TID DAMAGE EFFECTS ON SIGE HBTS ACROSS TEMPERATURE

#### 3.1 Introduction

Recently conceived projects in space exploration target extremely high speed data transmission from satellites for scientific investigation of outer planets and their moons . With emphasis on high fidelity data coupled with faster data rates, size-weight-and-power (SWaP) trade-offs become increasingly challenging to overcome. Burden is placed on the electronics to consume extremely low power and area while maintaining acceptable performance. In addition, such electronics must be insensitive (or at least predictable) to wide temperature swings and high levels of background radiation in space.

Existing systems rely on discrete commercial, off-the-shelf (COTS) components. These systems typically utilize a warm box to ensure reliable operation regardless of external temperature. The warm box is also used to protect the electronics from some radiation. While effective, the choice of COTS in a warm box results in very high SWaP. COTS tend to be bulky, leading to integration challenge. Warm box tends to be heavy, and maintaining constant temperature requires additional power.

To overcome the disadvantages described, this experiment aims to examine the feasibility of a fully integrated approach by SoC without a warm box. This system should be robust to temperature variation and radiation. It is proposed that SiGe technology is a promising candidate for such electronics.

State-of-the-art SiGe HBT processes present excellent performance at reasonable cost and manufacturability. Existing literature has also shown SiGe's relative hardness to TID. At the same time, SiGe performance improves at lower temperature, so an additional heating system is not required. However, even at high temperature, SiGe has been shown

Table 3.1: GlobalFoundries 9HP Specifications

Parameter	Value
Emitter Stripe Width	90 nm
$\beta$	500 A/A
$f_T$	300 GHz
$f_{MAX}$	350 GHz
$BV_{CEO}$	1.65 V

to maintain modest performance. Furthermore, SiGe BiCMOS technologies integrate both SiGe HBTs and silicon CMOS, allowing seamless integration of millimeter-wave (mm-W), radio frequency (RF), analog, and digital components.

In order to study SiGe’s capability for space systems, this study investigates the interaction of cryogenic temperatures with ionizing dose. By simultaneously controlling temperature and dose, the underlying physics of SiGe under extreme environment can be understood. With this knowledge in hand, corresponding compact models can be developed which will allow designers to predict circuit and system performance in the space environment. This will enable direct design targeted for space applications, drastically reducing SWaP compared to legacy approaches.

## 3.2 Experimental Samples

### 3.2.1 Silicon Germanium Technology

GlobalFoundries BiCMOS9HP (9HP for short) platform was chosen for this study. 9HP is a 4th-generation SiGe platform, offering the best commercially available performance in the US at a 90 nm lithography node. DC current gain ( $\beta$ ) is 500 A/A. Unity current gain cutoff frequency ( $f_T$ ) and unity power gain cutoff frequency ( $f_{MAX}$ ) are 300 GHz and 350 GHz, respectively. Open-base collector-to-emitter breakdown voltage ( $BV_{CEO}$ ) is 1.65 V. These specifications are summarized in Table 3.1.

The 9HP process design kit (PDK) features a wide variety of RF passives. Models for resistors, inductors, and capacitors, include parasitic components for broadband schematic

simulation accuracy. Parameterized layout cells remove the need to draw complicated geometries manually. Layout parasitic extraction can further improve simulation accuracy. In addition, the PDK allows integration with commercial electromagnetic (EM) simulators to capture high-frequency coupling between neighboring routes or components.

For added utility, the PDK also includes a suite of other active devices, including nMOS, pMOS, PIN diodes, varactor diodes, and Schottky barrier diodes. These devices improve the application space for which 9HP may be used.

### 3.2.2 Device Samples

To understand the physics of the SiGe HBT subject to simultaneous cryogenic temperature and TID (caused by gamma radiation in this experiment), individual transistors were examined. An emitter geometry of  $0.1 \times 2 \mu\text{m}^2$  was chosen to reflect the transistors used in the LNA also examined. By first observing the performance changes in a single device, conclusions can be drawn about potential changes in LNA performance.

The device samples and LNA were fabricated on the same silicon die. This ensures fair correlation of device performance to LNA performance. Three contacts for collector, base, and emitter were included to allow independent control of all electrical terminals on the single device.

### 3.2.3 Low Noise Amplifier

To eliminate the potential uncertainty of complex LNA topologies, the selected LNA is a standard cascode LNA. Its schematic is shown in Figure 3.1. Transistor  $Q_1$  is a transconductor and converts the input voltage swing into a current swing.  $Q_2$  acts as a current buffer, boosting maximum available gain and reverse isolation.  $Q_2$  also serves to minimize the Miller effect on the parasitic collector-base capacitance of  $Q_1$ , improving the amplifiers bandwidth. Inductor  $L_E$  is used to achieve simultaneous power and noise matching.  $L_C$ ,  $C_C$ , and  $R_C$  are a resonant tank which sets the bandwidth and output matching.

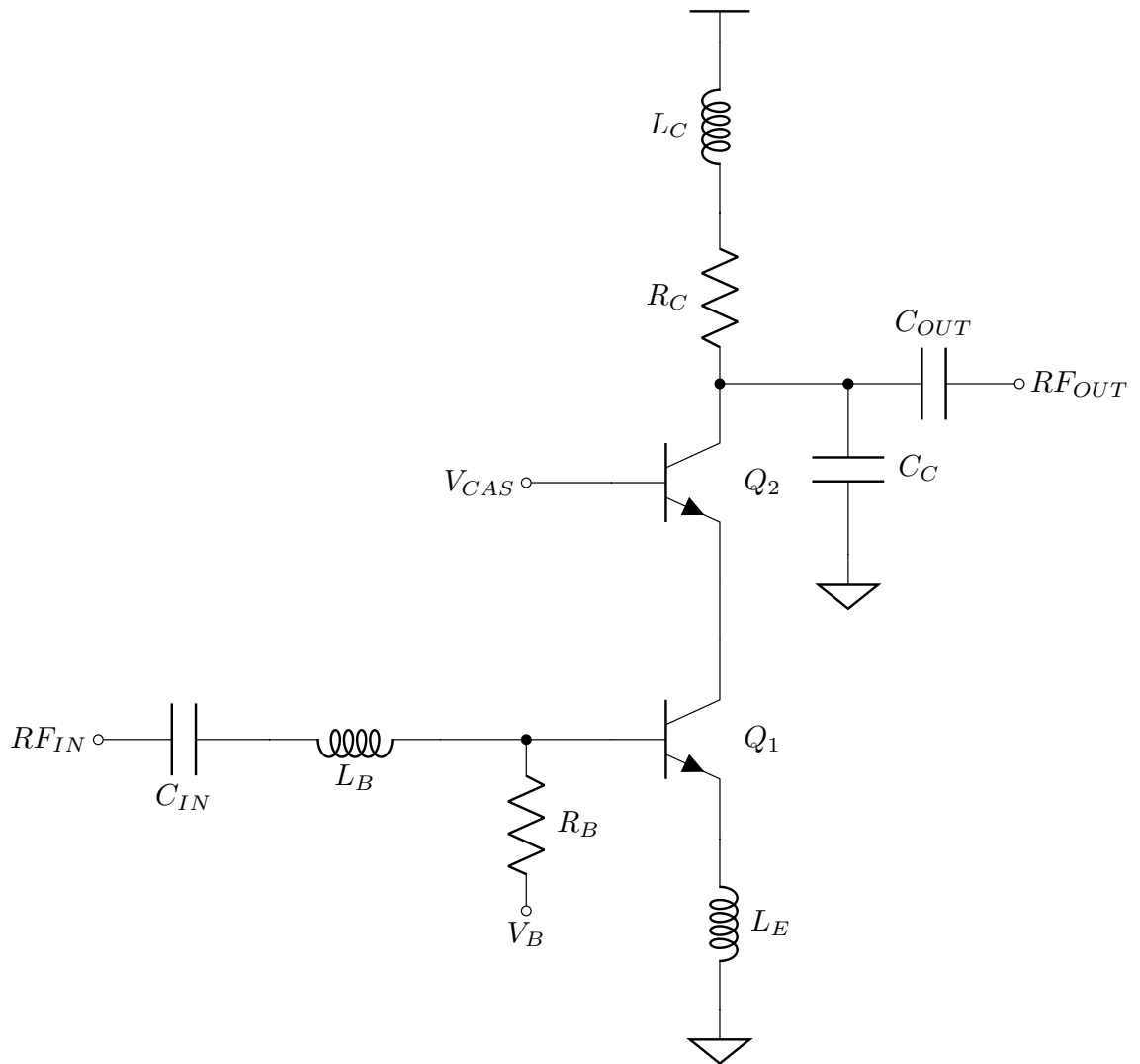


Figure 3.1: Schematic of the LNA under test.

RF passives were selected from the PDK. High-resistivity polysilicon was used for resistors. These resistors demonstrate negligible temperature coefficient. Planar spirals with patterned ground shielding was used for high-Q inductors. Metal-insulator-metal capacitors were used for high capacitance density.

The designed LNA targets S-band, with narrowband performance centered on 2.4 GHz. An example application of interest is the International Space Station, which uses S-band to communicate with the Space Shuttle.

### **3.3 Measurement Setup**

#### **3.3.1 System Configuration**

In order to perform DC and RF measurements, a custom printed circuit board (PCB) was designed to enable four-wire sense and real-time, in-situ RF calibration. To achieve this, off-the-shelf single-pole 8-throw (SP8T) switches were used. Switch connections were wire-bonded to pads on the PCB. Some paths of the SP8T were connected to short, open, load, and thru to enable SOLT calibration in-situ and in real time. Equalized line lengths were used to perform RF calibration to the device-under-test (DUT). The remaining SP8T paths were used for RF connection to the DUTs. A system diagram of the PCB is shown in Figure 3.2.

2.4 mm compression mount connectors were used for RF input and output. DC connections were tied to header pins to allow DC biasing of DUTs and the SP8T switches. Surface mount resistors and capacitors were used as bias tees to bias the paths of the SP8T. Extensive via stitching was applied throughout the PCB for maximum RF isolation. The bill-of-materials for the PCB is listed in Table 3.2.

The PCB was fabricated by Sierra Circuits. Rogers 4350B dielectric material was selected for its low loss up to mm-W frequencies. Trace widths were selected on the top metal layer to create  $50\ \Omega$  transmission lines. Four metal layers were used to provide excellent isolation between RF and DC lines. The top surface of the PCB was plated with soft gold

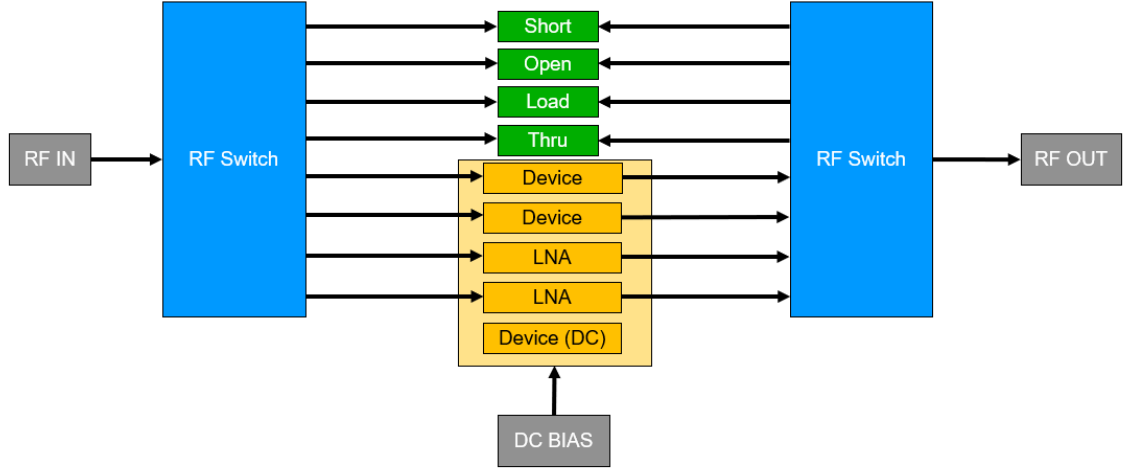


Figure 3.2: System diagram for the measurement configuration.

Table 3.2: Bill-of-Materials

Component	Vendor	Part Number	Count per Board
SP8T	Macom	MA4AGSW8-1	2
50 $\Omega$	Vishay	FC0402E50R0BST1	2
1 k $\Omega$	Vishay	TNPW06031K00BEEA	18
0.1 $\mu$ F	American Technical Ceramics	530L104KT16T	18
0.82 $\mu$ F	Murata	GRM155C80J82ME15D	8
2x12 DC Header Pins	—	—	1
2.4 mm Surface Mount Connector	SV Microwave	SF1621-60026-1S	2



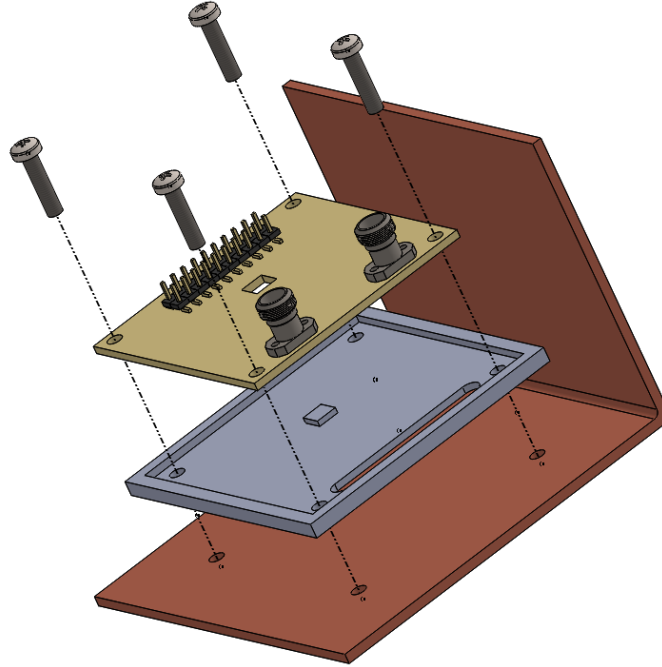


Figure 3.3: Exploded view of PCB (top), aluminum interposer (middle), and CryoTiger cold plate (bottom).

to allow wire-bonding from the board to pads of the DUTs.

External dimensions and features of the PCB were carefully designed for compatibility with JPL’s vacuum mini-chamber (CryoTiger) that allows for electronics to be tested under low-temperature conditions while irradiated. An internal cutout was created for placement of the DUTs. This enabled proper thermal contact of the DUTs to the cold head of the CryoTiger, ensuring accurate temperature control at the DUT. A custom aluminum interposer was designed to electrically isolate the PCB from the cold head while maintaining enough thermal conduction. An exploded 3-D rendering and photograph of the overall construction are shown in Figs. 3.3 and 3.4. A photograph of the PCB construction embedded in the CryoTiger is shown in Figure 3.5.

To enable rapid and accurate selection of SP8T paths and DUT biasing, a custom switch box was designed. Coaxial and triaxial connectors were used to interface test equipment to the DUTs. Mechanical switches were point soldered to form DC connections, minimizing the chance of operator error. A photograph of the switch box is shown in Figure 3.6.

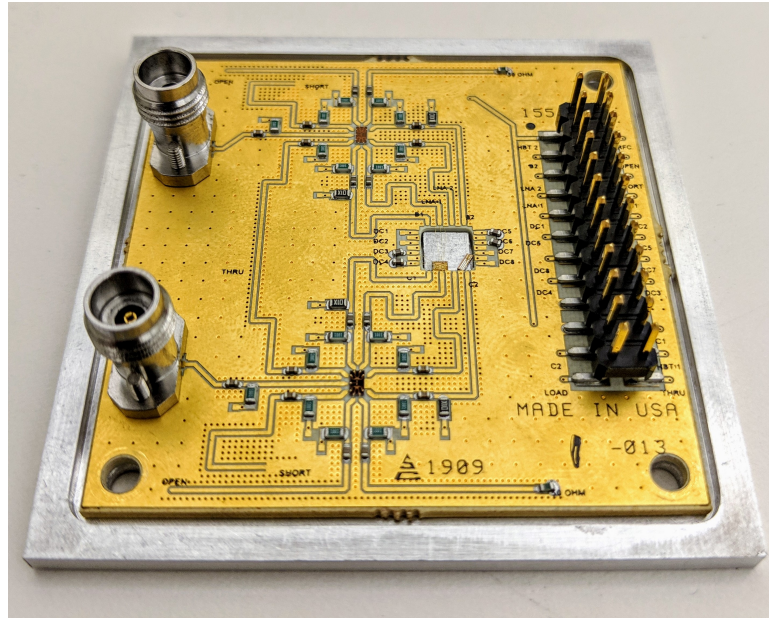


Figure 3.4: Real photo of the PCB mounted to the aluminum interposer with DUTs wire-bonded to the PCB.

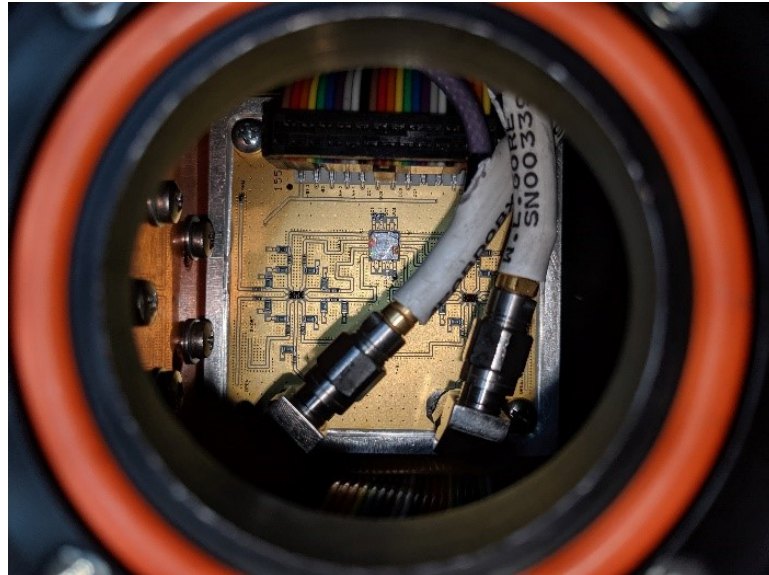


Figure 3.5: PCB construction viewed through CryoTiger radiation window. Internal RF cables used to connect to vacuum chamber port. Ribbon cable for DC connection.

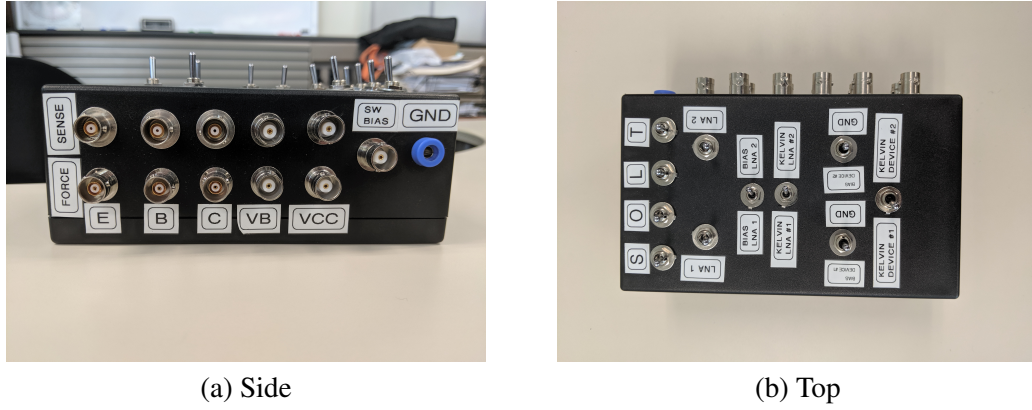


Figure 3.6: Custom designed switch box when viewed from the (a) side and (b) top.

### 3.3.2 Device Measurements

HBTs are classically characterized by their Gummel characteristic. Collector current ( $I_C$ ) and base current ( $I_B$ ) are plotted against base-emitter voltage ( $V_{BE}$ ). Ideally, this gives an exponential dependence. This also gives the DC current gain,  $\beta$ , as the ratio of  $I_C$  to  $I_B$ . TID tends to increase trap concentration in the oxide near the base-emitter junction, leading to increased  $I_B$  and consequently degraded beta. Thus, the Gummel characteristics serve as direct demonstration of TID damage.

The Gummel characteristics of the inverse-mode device can be measured as well. In this case, the physical collector and emitter terminals are swapped. While inverse mode suffers worse performance, both AC and DC, it helps in the investigation of device physics. Degradation in inverse mode is instead caused by damage near the physical collector-base junction (refer to Fig. 2.4). Measurement of both forward and inverse Gummel characteristics can therefore isolate regions of damage.

For all the above measurements, the Agilent 4156C Semiconductor Parameter Analyzer is used. The 4156C features four source-measuring units (SMUs) that are used to control the terminals of the transistor. Four-wire force-sense is used to eliminate the effects of unwanted series resistance from cabling. Automatic sweeps are configured to generate Gummel characteristics.

### 3.3.3 LNA Measurements

The LNA was characterized for small-signal, noise, and linearity performance. Small-signal S-parameters were measured with the Agilent E8363B vector network analyzer (VNA). This gave the gain, matching, and reverse isolation performance. VNA calibration was performed using the custom on-board SOLT standards.

Noise figure (NF) measurements were performed with the Agilent E4470B ESA-E spectrum analyzer with the noise figure personality. Hot and cold noise powers were generated with the Agilent N4002A smart noise source. For cross verification, the Agilent 346C noise source was used as well. The standard Y-factor method was used to extract noise figure. Cable loss was carefully calibrated, including the effects of having multiple temperatures in the signal path.

For all LNA measurements, bias conditions were swept. Since the HBT is fundamentally a current-driven device, all LNA samples were biased at the same set collector currents. Various collector currents were used to investigate the dependence of LNA performance on bias level. LNA biasing was done with Keithley 2400 Source Meters.

### 3.3.4 In-Situ Measurement Methodology

A major focus of this experiment was to isolate the effects of temperature on the degradation due to TID. Theoretically, a lower temperature decreases charge yield [31], so cryogenic operation should mitigate TID damage. A challenge arises because the SiGe HBT naturally improves in performance with decreasing temperature. Thus, a method is required to decouple changes in performance due to temperature and TID.

To achieve this decoupling, different samples were irradiated at 120 K and 300 K, then measured at 120 K, 200 K, and 300 K. In this way, the intrinsic effect of temperature on performance could be controlled. Any remaining difference in performance could then be attributed to TID damage. Further, to study trends over increasing dose, the cycle of measuring at three temperatures was performed at 100 krad(Si), 500 krad(Si), and 1000

krad(Si).

During in-situ measurement, the Neocera LTC11 temperature controller was used to adjust temperature. A Cernox 1050 HT temperature sensor was used as a temperature monitor and was mounted on the bottom of the cold plate on one of the screws that held the cold-plate and the aluminum interposer. Two separate thermocouples were also installed on the bottom of the cold-head on opposite sides of the Cernox temperature sensor to monitor temperature gradients across the cold-plate. Once the desired temperature was reached and stabilized across all three temperature sensors, the measurements were started. The temperature on all three sensors was monitored during the measurement for signs of self-heating within the device. Self-heating was not observed as the temperature remained constant throughout the measurements. For a radiation source, the Co-60 lab at JPL was used. Dosimetry measurements were taken before initiating the experiment to verify dose rate.

### **3.4 Device Measurement Results**

#### **3.4.1 TID Damage in SiGe HBT At Room Temperature**

Interaction of photons with SiO<sub>2</sub>, leaves behind EHPs in the oxide that are usually trapped, or “stuck”. Holes have several orders of magnitude less mobility in the oxide compared to electrons. When EHPs are generated, electrons are quickly swept away, leaving an excess of holes, and a net positive charge, in the oxide. The photons can also cause Si-SiO<sub>2</sub> passivated bonds to break, leading to interface defects [32]. Charge trapped in the SiO<sub>2</sub> will alter any bulk depletion region that surrounds it, while defects on the Si-SiO<sub>2</sub> interface will generate surface traps that will alter current flow.

A SiGe HBT will typically have two main oxides that play a critical role in the device’s transport physics when irradiated. Again refer to Fig 2.4 for the physical location of these oxides.

From Shockley-Read-Hall generation/recombination theory, when traps are present in

the depletion region of a forward-biased junction, an extra leakage current must be supplied by the base terminal in order to maintain charge neutrality. When the HBT is operated in the forward mode ( $V_{BE} > 0$  and  $V_{BC} < 0$ ), the EB-spacer is the oxide that causes the leakage current. EB-spacer damage is shown in Figure 3.7a as an increase in base current in the forward Gummel characteristics.

On the other hand, when the HBT is operated in the inverse mode, ( $V_{BE} < 0$  and  $V_{BC} > 0$ ), the STI is the oxide that contributes increasing leakage current. STI damage is shown in Figure 3.7b as an increase in base current in the inverse Gummel characteristics.

Measuring both forward and inverse mode helps isolate the physical locations of damage in the device.

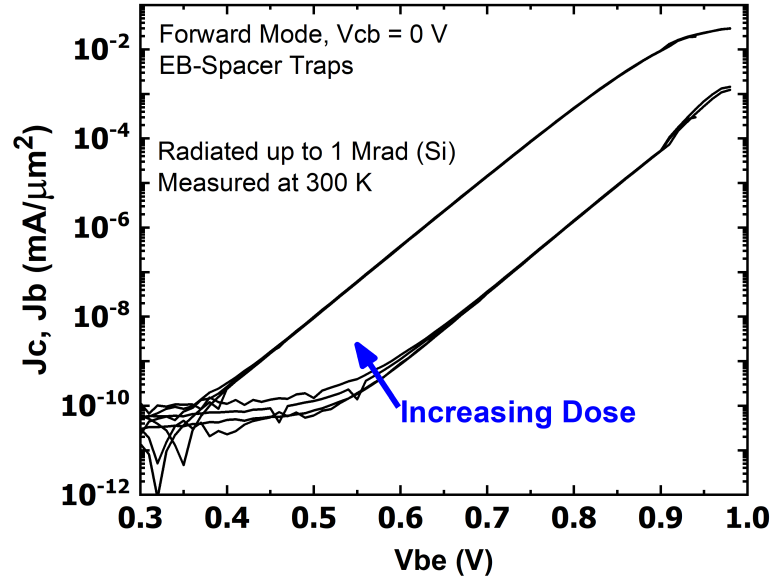
### 3.4.2 TID Damage Measured Across Temperature

To understand what happens to the damage in a SiGe HBT across temperature, the samples were cooled down to 120 K, with measurements at 300 K, 200 K, and 120 K. The forward and inverse Gummel characteristics pre- and post-radiation are shown in Figure 3.8 with post-radiation at 1 Mrad (Si).

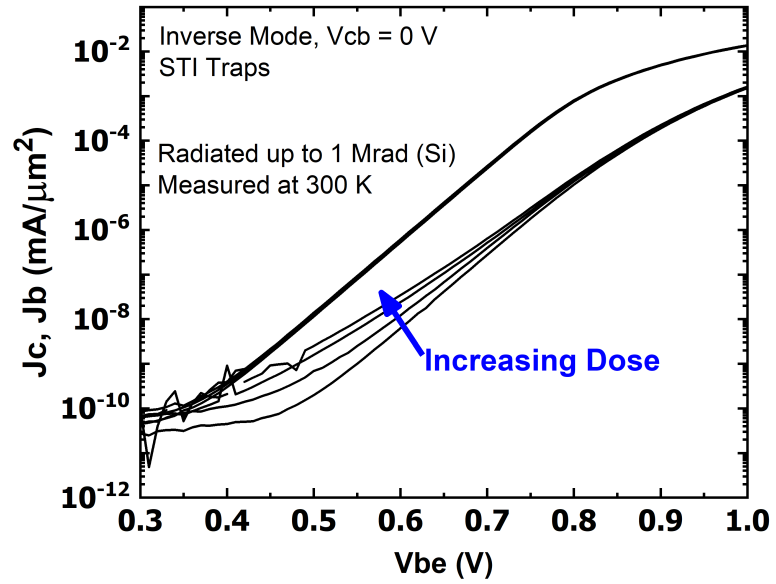
As the temperature decreases, the slope of the IV characteristics increases because there is an exponential relationship between temperature and the amount of current flowing through the device at a given voltage. It is more pronounced in the inverse Gummel, but it seems like the same amount of damage (density of traps) has less effect in leakage current at lower temperatures.

A plot of the change in base current post/pre, shown in Figure 3.9, shows that TID damage is most noticeable at higher temperatures in the inverse Gummel. This could be due to the fact that the trap capture coefficient (i.e., the effect of a trap on a carrier) is decreasing as the temperature is decreasing. In other words, identical trap densities get suppressed at low temperature.

Another important phenomenon is that damage is more observable in the inverse Gum-

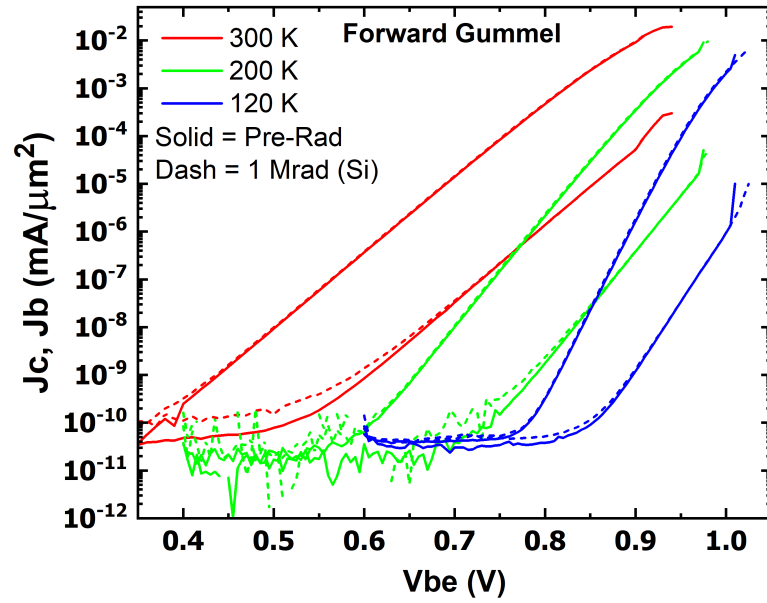


(a) Forward Gummel

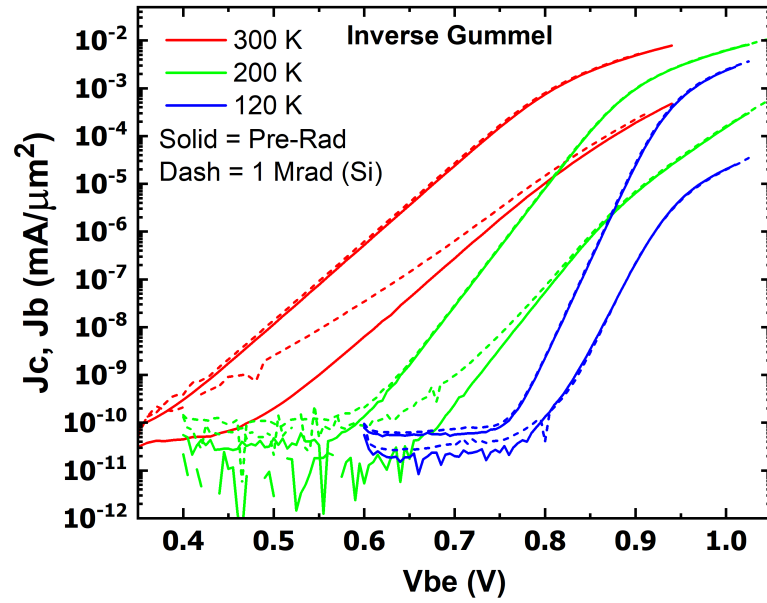


(b) Inverse Gummel

Figure 3.7: Comparison of forward and inverse mode damage. (a) Damage accumulation due to traps in the EB-spacer. (b) Damage accumulation due to traps in the STI.



(a)



(b)

Figure 3.8: Comparison of (a) forward and (b) inverse Gummel characteristics over temperature. The inverse Gummel shows more when damage measured at 300 K, but at 120 K almost all of the damage is hidden.



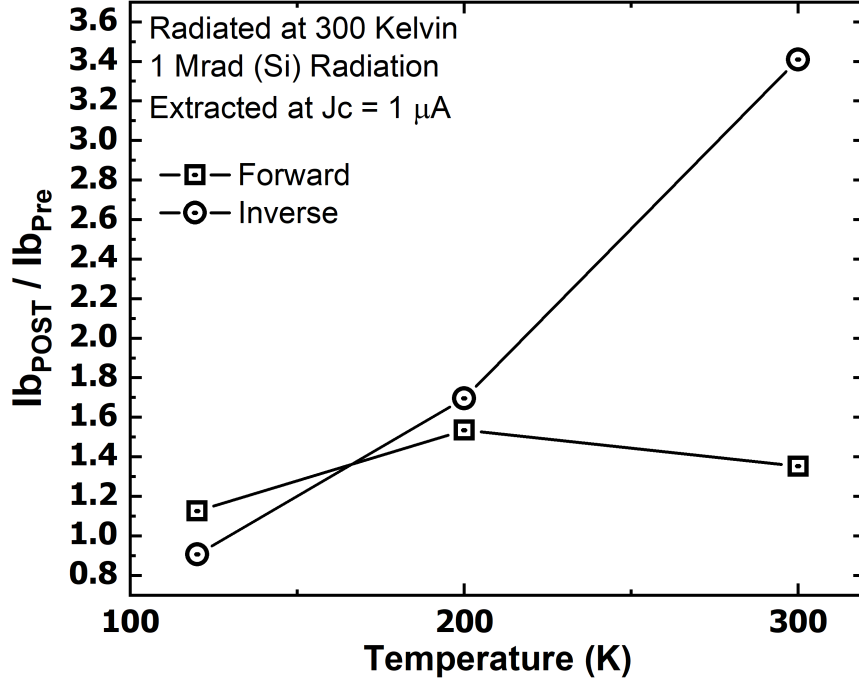
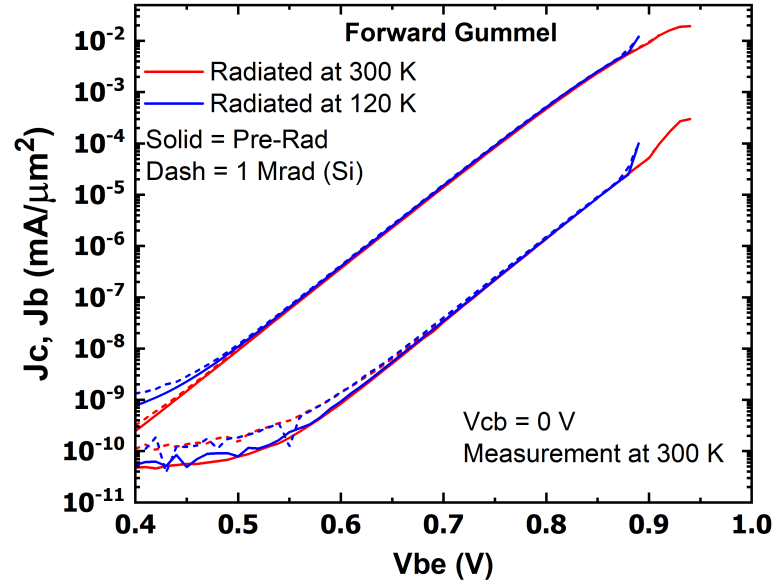


Figure 3.9: Comparison of apparent damage at different temperatures showing less apparent damage at low temperature.

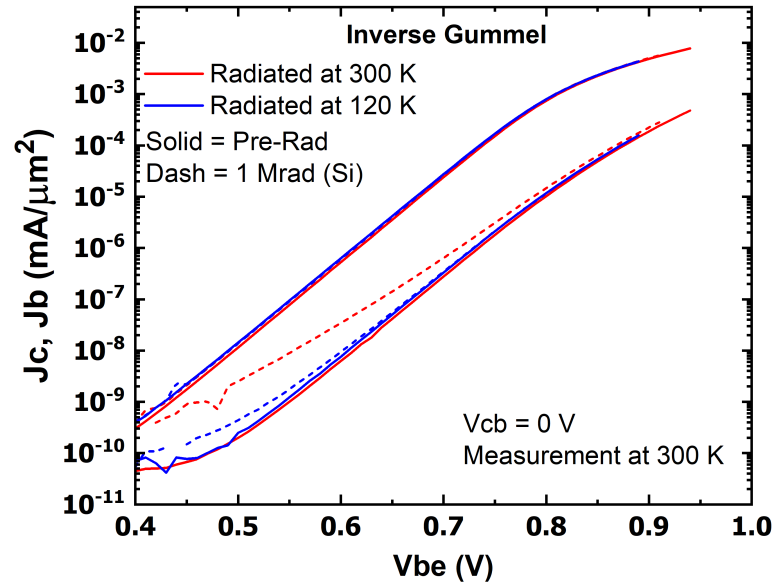
mel than the forward Gummel. This is likely because the space charge region around the EB-spacer is much smaller than the space charge region around the STI due to several orders of magnitude higher doping in the emitter than the collector. Note that it is not necessarily “more” damage in the STI than the EB-Spacer, rather, the damage in the STI has more of an effect in the inverse Gummel compared to the damage in the EB-spacer on the forward Gummel.

### 3.4.3 TID Damage When Radiated at Different Temperatures

The previous section dealt with how the damage appears in a SiGe HBT radiated at a single temperature (300 K) measured at various temperatures. This section will deal with how much damage is actually present when a SiGe HBT is radiated at a different temperature. It was also seen that with the same amount of damage, depending on the operating temperature, the effect of that damage will vary. Thus, it is important that the post radiation measurement temperature is identical when comparing the damage yield of two devices



(a)



(b)

Figure 3.10: Comparison of (a) forward and (b) inverse Gummel characteristics when irradiated at different temperatures.

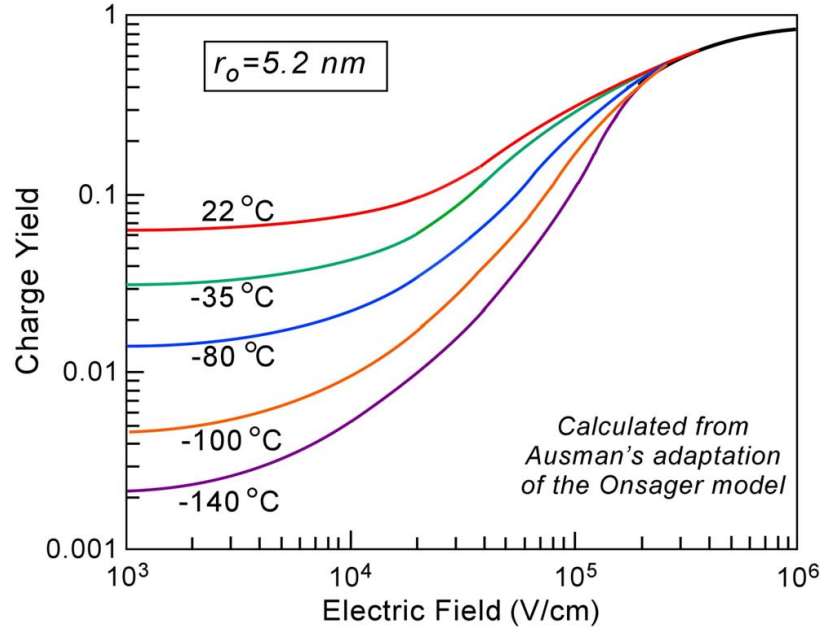


Figure 3.11: Charge yield at different temperatures and electric fields [31].

radiated at different temperatures.

Fig. 3.10 shows two identical SiGe HBTs that were irradiated at 300 K and 120 K but measured pre- and post-radiation at 300 K. From inspection, it can easily be seen that the inverse Gummel shows that the device that was radiated at 300 K has accumulated more damage than the device that was radiated at 120 K. However, in the forward Gummel, the damage appears to be identical. This can be explained by the temperature and field dependencies of charge yield (i.e., damage per dose) in  $\text{SiO}_2$  from highly energized gamma rays. Johnston et al [31] showed that when a gamma ray creates an EHP in  $\text{SiO}_2$ , the EHP has to be separated at some minimum distance to contribute to the overall charge in the oxide. If the electron and hole do not get separated by that minimum distance, they will simply recombine, and no charge will be added to the oxide.

There are two main methods of charge separation once a gamma ray creates an EHP. The first being field dependent. If an electric field exists at the spatial point where the EHP is created, then that field will do work in accelerating the electron in one direction and the hole in the other direction. The second being temperature dependent. A crystal will

naturally contain some amount of thermal energy at equilibrium seen as lattice vibrations, or phonon scattering, which can naturally shove particles away from each other.

The charge yield dependence on electric field and temperature is shown in Figure 3.11. Notice that at sufficiently high electric fields, the charge yield becomes temperature insensitive. The temperature dependence is only present at low electric fields.

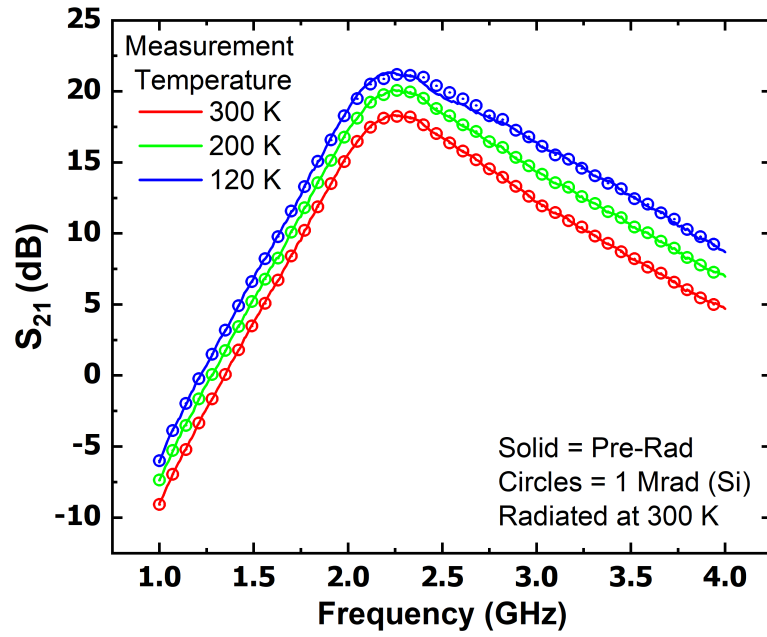
In the SiGe HBT, the EB junction is doped at relatively high amounts of doping. This means that the electric field that extends inside the EB-spacer is relatively high. On the other hand, the CB junction is doped at several orders of magnitude lower, so the electric field magnitude that extends in the STI is much lower than the EB-spacer. This explains why the damage in the forward Gummel is more identical across temperature, while the damage in the inverse Gummel is much higher for an identical dose that was delivered at a higher temperature.

### 3.5 LNA Measurement Results

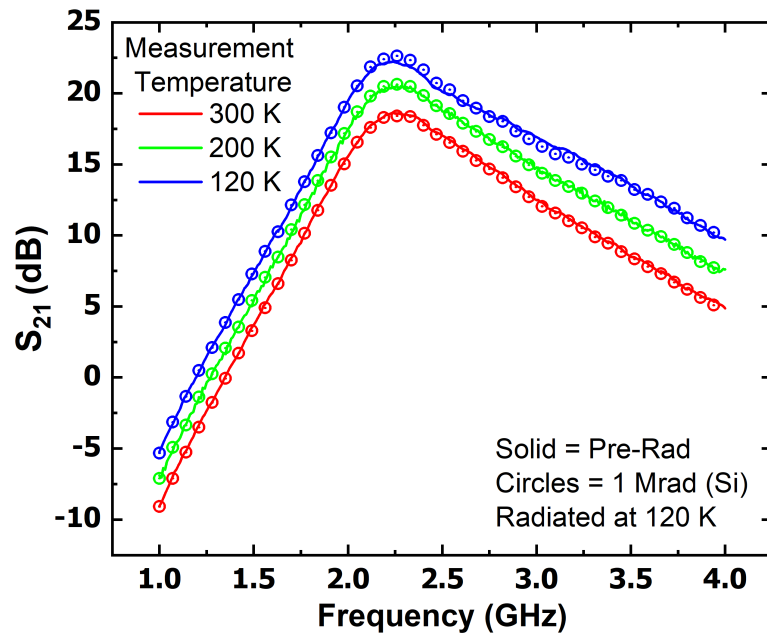
#### 3.5.1 TID Effects on LNA Gain

Two identical SiGe LNA's were also irradiated and measured at different temperatures. Shown in Figure 3.12 are the results of pre- and post-radiated measurements of the  $S_{21}$  parameter (i.e., gain) of both LNAs. One thing that is very evident is that the gain of the LNA actually increases as the temperature is decreased. This is known and can be explained by the increased performance of SiGe HBTs at low temperatures (i.e., gain,  $f_T$ ,  $f_{MAX}$ ).

The damage created by 1 Mrad (Si) of TID in the LNAs, however, shows that there is negligible degradation in the LNA performance. This is because the current density through the SiGe HBTs in the LNA is greater than  $1.25 \text{ mA}/\mu\text{m}^2$ . This means that the LNA is biased in a regime where the TID damage on base current is negligible. While the assumption seems to hold true for this LNA, more studies are needed to be done on the TID effects on RF performance.



(a) 300 K



(b) 120 K

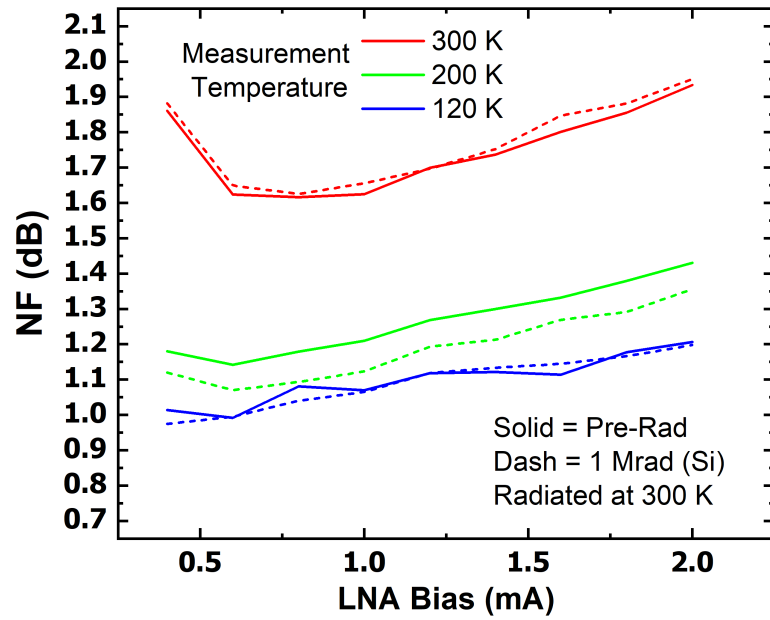
Figure 3.12: Comparison of gain when irradiated at (a) 300 K vs (b) 120 K.

### 3.5.2 TID Effects on LNA Noise Figure

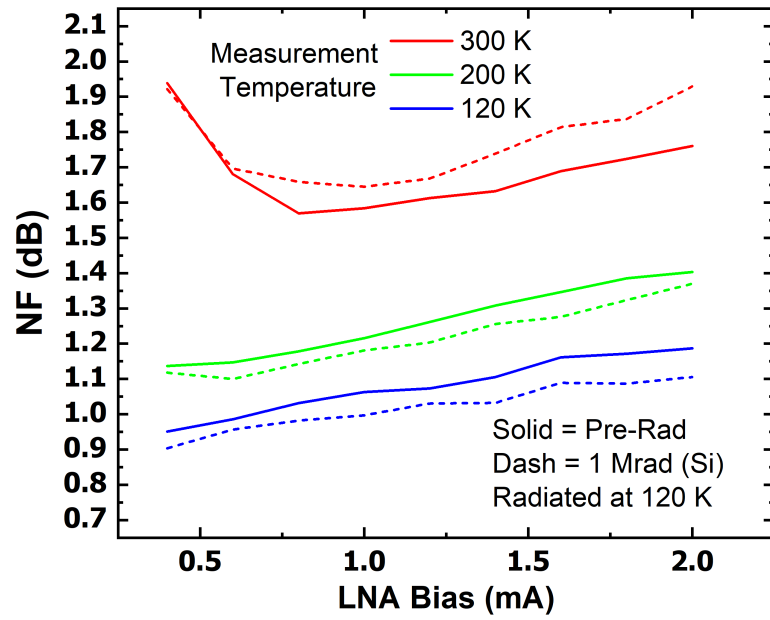
One of the most important parameters of LNA performance is how much noise the LNA itself produces on top of a signal, namely, its NF. Less NF is obviously better. Shown in Figure 3.13 is the NF across LNA bias for 2.4 GHz. Similar to the gain explanation, the NF reduces as the LNA is cooled; again, this is mainly due to the increase of device noise performance with decrease in temperature. It is also tempting to say that the NF changes with TID. However, a closer look will show that there is no statistically significant deviation from pre-radiation NF to post-radiation NF. This is because there were 5 measurements taken at each bias. The repeatability of each NF curve varied by about 0.15 dB. For example, in Figure 3.13b, the post-radiation curve at 300 K show that NF increases by about 0.1 dB. However, 200 K and 120 K measurements show the opposite trend. While for the LNA that was radiated at 300 K in Figure 3.13a, shows again a seemingly opposite trend.

The best conclusion one can draw out from these data, is that NF does not significantly degrade with TID up to 1 Mrad (Si). Furthermore, if NF is changing after 1 Mrad (Si) of radiation, it has to be changing by less than approximately 0.15 dB (which is below the resolution of our measurement setup).

This is actually a surprising result since noise is directly correlated to traps and imperfections along the transport paths of transistors. At this point, it is not obvious or clear as to why the NF is not at least increasing by noticeable amounts. A possible explanation is that the NF is dominated by some other process in the LNA, and the TID damage on the SiGe HBT is overcome by this other process. Another possible explanation (similar to the gain explanation) is that the transistor in the LNA is biased in the regime where leakage current degradation becomes negligible. While this seems like a satisfactory explanation, there should have been a deviation in NF pre- and post-radiation at lower LNA bias, but that is not observed in Figure 3.13. More work needs to be done on this issue to understand why TID radiation does not have a significant impact on the LNA NF.



(a) 300 K



(b) 120 K

Figure 3.13: Comparison of noise figure when irradiated at (a) 300 K vs (b) 120 K.

### 3.6 Summary and Future Work

Cold-capable, rad-hard electronics are seemingly becoming more important as deep space exploration missions require an ever decreasing SWaP-C while operating in higher dose environments (e.g., Jovian environments). SiGe HBTs have proven to be competitors over the past decade to try and fulfill these requirements [21], [20]. While much work has been done on understanding the radiation effects and temperature effects on SiGe HBTs separately, there has been very little work done in understanding both in a synergistic fashion. This is the first study aimed at understanding how TID and temperature play with one another inside of a SiGe HBT in the context of RF performance.

Measurement of RF characteristics presents a unique challenge. The addition of a vacuum system, cables, temperature variation, and TID necessitates extreme care to ensure proper calibration and de-embedding of desired measurements. Choosing a set of test parameters is also difficult. RF performance varies drastically with frequency and bias. Choosing the right ranges for sweeps to collect meaningful data over temperature and TID is a yet unexplored issue in this field.

We have shown that the SiGe HBTs used in this study are consistent with literature in that they exhibit improved dc and ac performance over temperature. We have also shown that TID up to 1 Mrad(Si) is at best negligible for SiGe devices especially in the context of the LNA where NF does not seem to degrade with radiation. It is also important to note that radiation exposure at lower temperatures show that there is a decrease in charge yield at the STI. This means that the SiGe HBTs not only intrinsically perform better at low temperatures, but also accumulate less damage at those lower temperatures.

This study was aimed as a first step to show that SiGe HBTs in fact do possess the strict performance metrics and harsh radiation tolerance needed for future deep space missions.



## **CHAPTER 4**

### **SET TRENDS IN SIGE HBTs ACROSS TEMPERATURE**

The previous chapter dealt with the TID response of SiGe technology at lower temperatures. This chapter tries to identify the vulnerabilities of SETs in SiGe technology at lower temperatures. Due to the incredible difficulty of placing parts that are cooled to cryogenic temperatures in front of a heavy-ion beamline, this chapter only provides an analysis that is within the simulation domain.

#### **4.1 Introduction**

In the previous chapter it was seen that TID causes less damage to SiGe HBTs at lower temperatures making SiGe technology a strong contender for electronics used in space missions such as to Jupiter and its moons. However, as described earlier, it is known that SiGe HBTs are highly susceptible and vulnerable to SETs. The logical question then is how do SETs show up in cooled SiGe HBTs? As it will be shown in following sections, SETs induced in SiGe HBTs at low temperatures typically show up as having a larger magnitude but a faster recovery time. By itself, it is difficult to determine whether or not these trends have a positive or negative affect when determining the probability of mission success. Therefore, two different circuit examples will be shown in this chapter to illustrate the competing trends of SETs generated in a device across temperature.

#### **4.2 Single Device SETs**

##### 4.2.1 Simulation Setup

A 3-D TCAD model of a SiGe HBT was designed in the NanoTCAD software suite developed by the CFD Research Corporation (CFDRC) [33, 34, 35]. It is desirable to calibrate

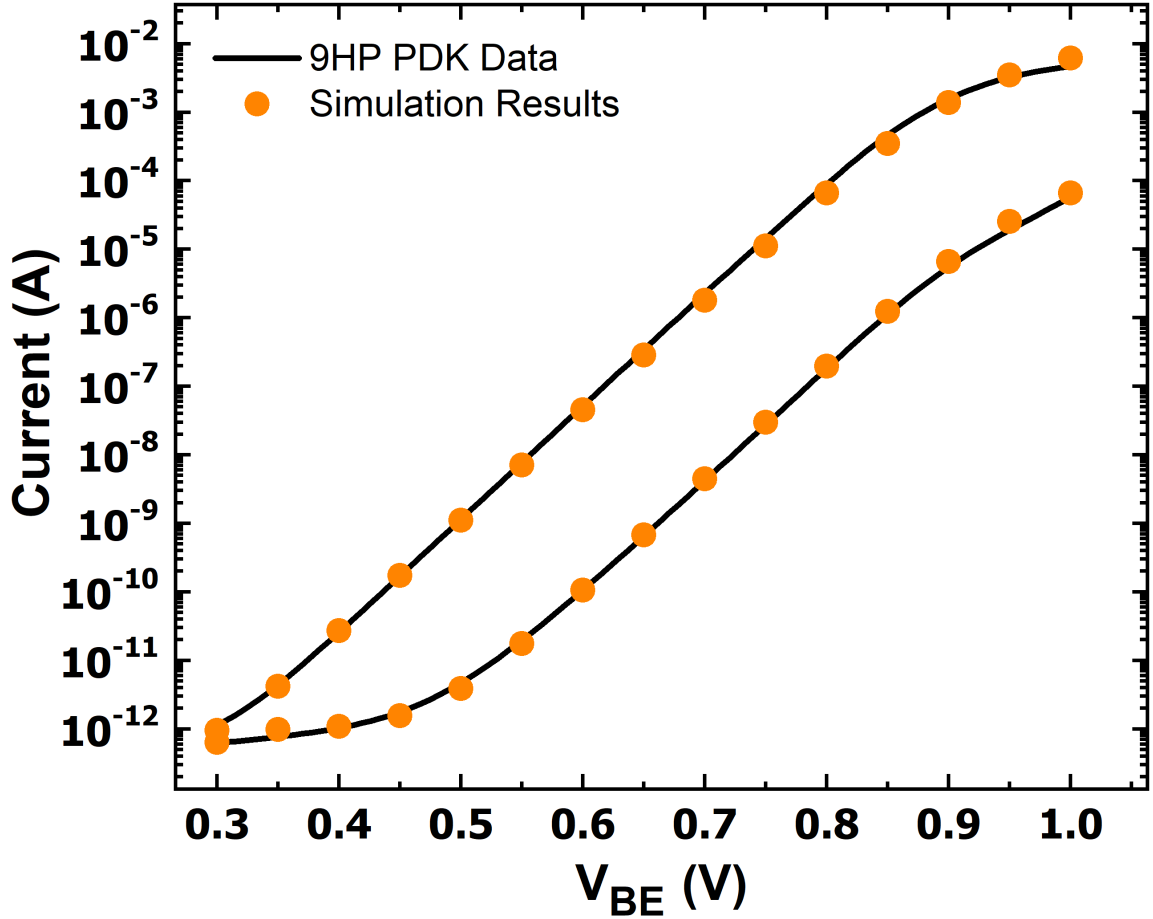


Figure 4.1: A comparison showing GF 9HP results from the PDK to the 3-D TCAD calibration used in this study.

the 3-D model to a known, measurable technology to enable a more robust analysis of the simulation results. The GlobalFoundries 9HP process was chosen since the previous study incorporated the same technology. The forward Gummel for the model and the PDK given results from the foundry is in good agreement and is shown in Fig. 4.1 for a  $0.1 \times 1 \mu\text{m}^2$  device.

The ion-strike simulations are configured such that a radially Gaussian generation of charge is generated vertically through the Emitter-Base-Collector-SubCollector-Substrate stack up where the device is known to be the most sensitive [21]. An example of such a simulation is shown in Fig. 4.2. An LET value of  $10 \text{ MeV}\cdot\text{cm}^2/\text{mg}$  was used since that is an intermediate LET value and provides transients large enough to show trends, but not too

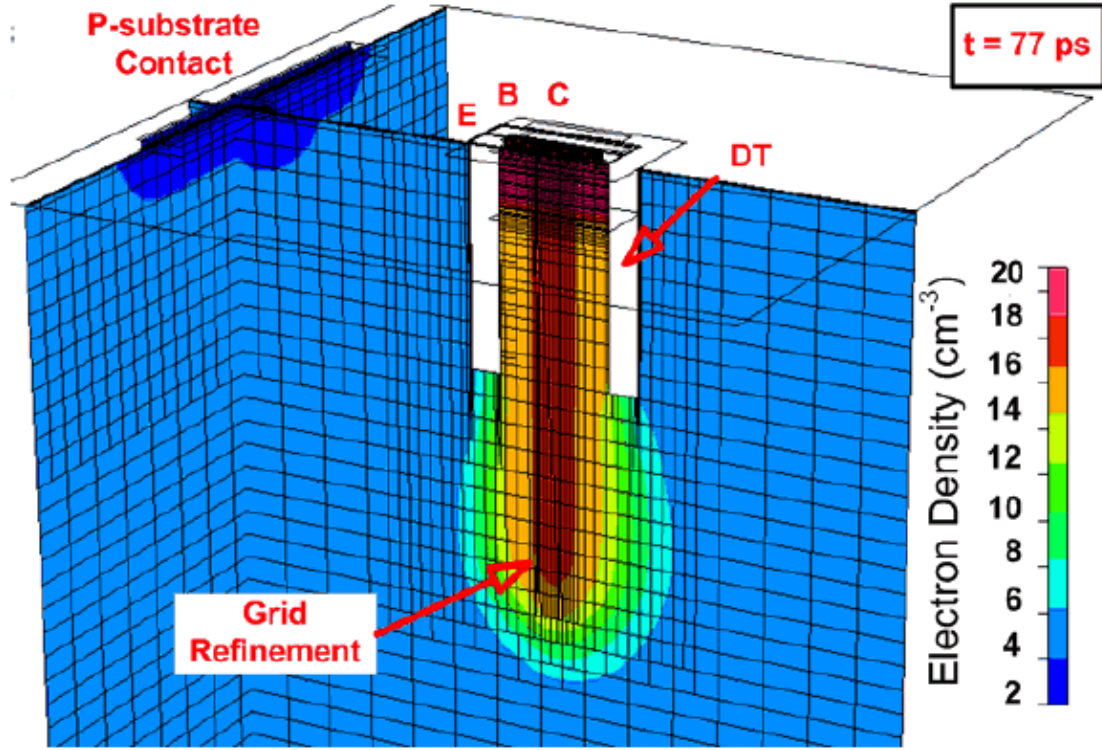


Figure 4.2: An example of ion-strike simulation captured immediately after the strike has begun. (Courtesy Dr. N. Lourenco)

large where the simulations are more difficult to converge.

#### 4.2.2 Device Transient Results

Fig. 4.3 shows the simulation results of emitter-centered transients ( $\text{LET} = 10 \text{ MeV-cm}^2/\text{mg}$ ) for two simulation temperatures: 300 K and 250 K. The device was biased the same for both cases with base-emitter voltage ( $V_{be}$ ) = 0.9 V and collector-base voltage ( $V_{cb}$ ) = 0 V. The simulation shows that the transient from the colder device is larger in terms of absolute magnitude but shorter in duration. This is due to the fact that the carrier mobility at colder temperatures rises thereby making the charge collection process faster for the generated carriers [36, 37]. Faster charge collection means that the carriers have less of a probability to recombine and can reach the terminals of the device easier increasing the peak of the transient.

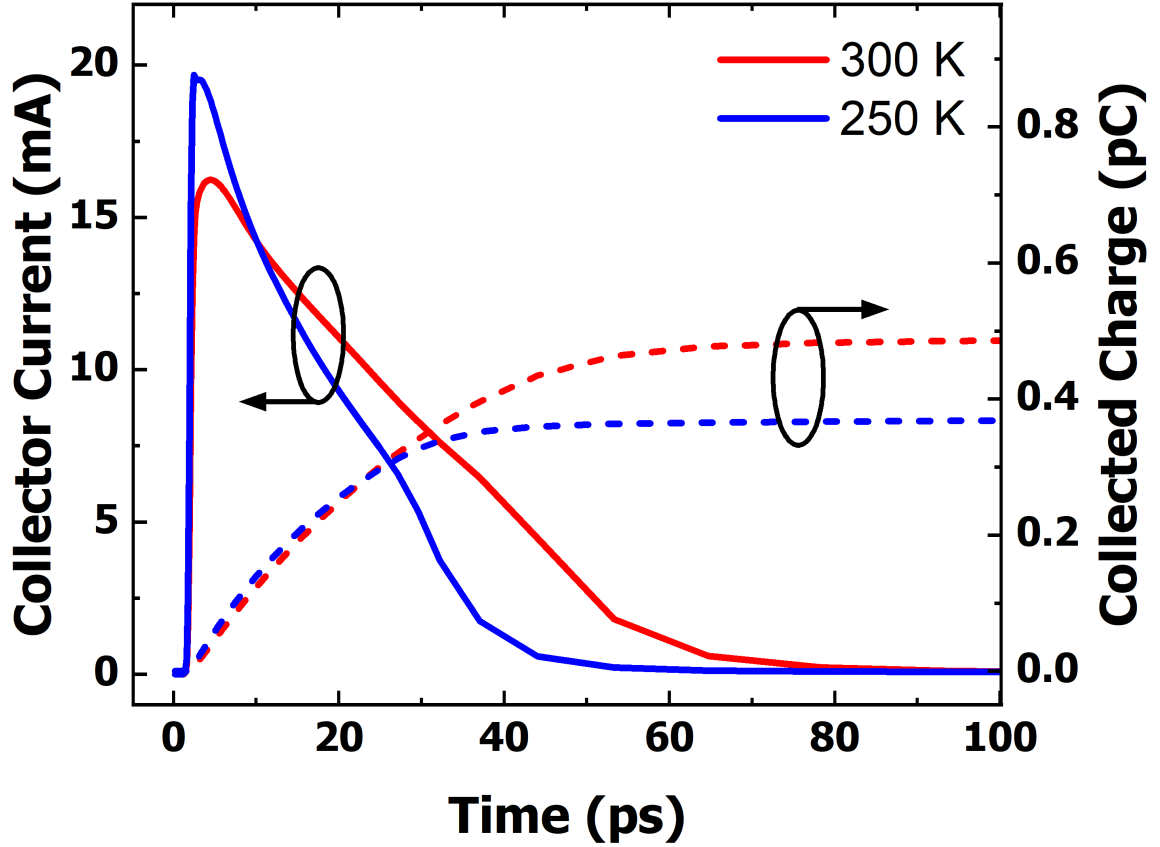


Figure 4.3: Simulation results showing the transient induced in a SiGe HBT by a heavy ion with  $LET = 10 \text{ MeV-cm}^2/\text{mg}$  at 300 and 250 K.

The tail portion of the transient in SiGe HBTs has been studied before in detail and attributed to charge collection from deep within the substrate through the subcollector-substrate junction [38, 14, 39]. It is believed that the reason there is a decrease in duration from the “colder” transient is again due to the increased mobility of charges getting collected faster. Furthermore, as depicted in Fig.4.3, there is less overall charge collected by the device. This is potentially due to the fact that the EHPs generated in the substrate at colder temperatures easily diffuse and recombine away from the device. So the fraction of EHPs that get collected as part of the tail are the ones that happened to diffuse towards the device.

### 4.3 Circuit-Level SETs

To get a better understanding of the impact of SETs on circuits that are operating at lower temperatures, the simulations were extended in a true mixed-mode environment. The NanoTCAD simulation suite offers the ability to incorporate the developed model for the transistor (as well as other electrical components) into SPECTRE, which is an all-encompassing electrical circuit and system signal simulator within the Cadence software suite [40]. This allows for a realistic circuit to be designed with all of the PDK specifications for active and passive components. Once the circuit is designed, the calibrated model developed in NanoTCAD can be replaced for one of the devices, and a full mixed-mode ion-strike simulation can be performed.

#### 4.3.1 Circuit Selection

The circuit used for this study is 2.4 GHz narrowband LNA that was designed and fabricated by GlobalFoundries in the 9HP high-performance platform. A schematic of this circuit is shown in Fig. 4.4. For more information about the performance metrics and the specific values used for passives in this study refer to [41, 42]. The circuit was chosen for two reasons: 1) it was designed specifically to be used for radiation effects studies, and 2) once the capability to test RF circuits at low temperatures while simultaneously receiving heavy-ion radiation is developed, this circuit can easily be tested to further understand the simulation results shown in this chapter.

The studies in [41, 42] specifically focus on the use of inverse mode as an radiation-hardening-by-design (RHBD) technique. The operation of a transistor in inverse mode is said to suppress the SET vulnerability by trading off a little performance in the actual transistor. For this work, the inverse mode simulations will also be shown to determine if the same trend holds true for low temperatures. For more information on inverse mode operation of SiGe HBTs as an RHBD technique, the reader is referred to [43] as an initial

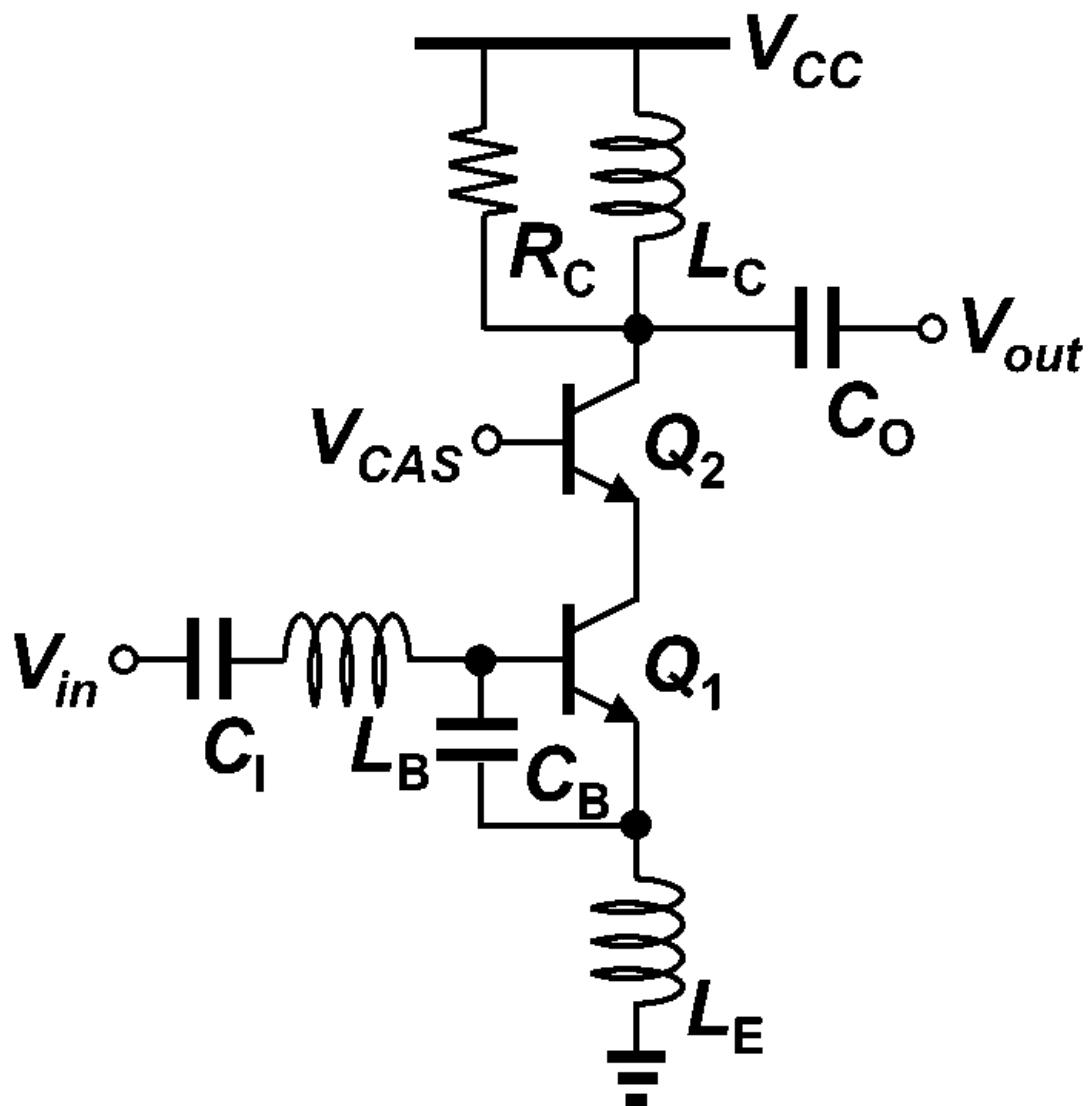


Figure 4.4: The circuit schematic of the LNA for this study. (Courtesy Dr. I. Song)

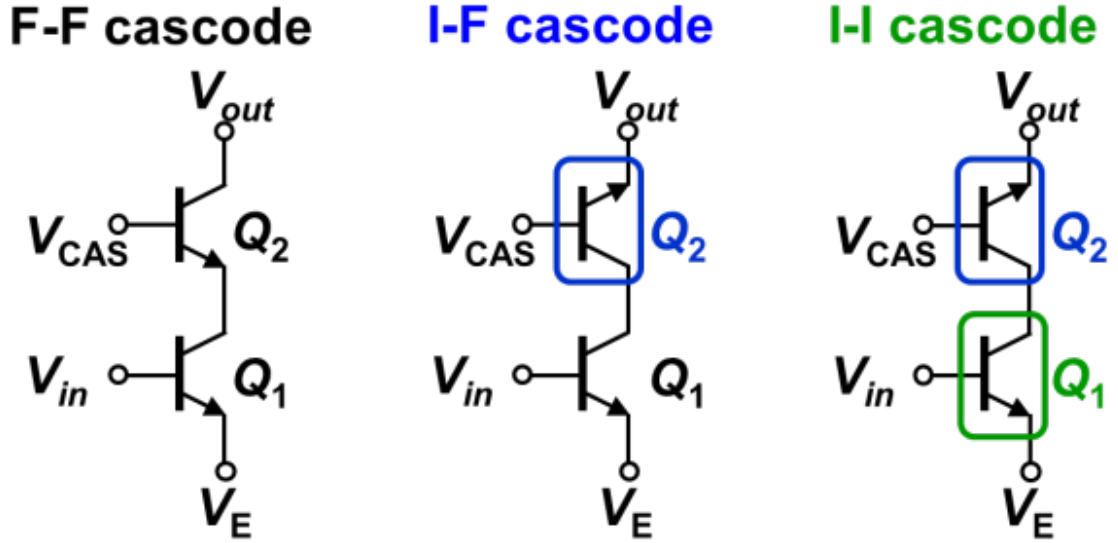


Figure 4.5: The three configurations for inverse-mode use in the LNA. (Courtesy Dr. I. Song)

work on this topic, and then in chronological order [44, 45, 46, 41, 42] for follow-on studies.

The three variants for the common-emitter device ( $Q_1$  or CE) and the common-base device ( $Q_2$  or CB) transistor configurations are forward-forward (FF), inverse-forward (IF), and inverse-inverse (II) as shown in Fig. 4.5. All of the following transient simulation results that are shown are from the transistor  $Q_1$  being struck by a heavy ion with  $LET = 10 \text{ MeV-cm}^2/\text{mg}$ . The  $Q_2$  output buffer transistor shows no considerable transients after ion strikes since its operation is current limited and exhibits no gain in the circuit [47], and is thus omitted from this study.

#### 4.3.2 LNA Circuit Transient Results

##### *FF Configuration*

The first step to verify if the simulator can produce realistic results is to verify the simulation data with measurement data. Therefore, mixed-mode simulations using the NanoT-CAD and SPECTRE simulation tools were performed on the LNA to compare the results

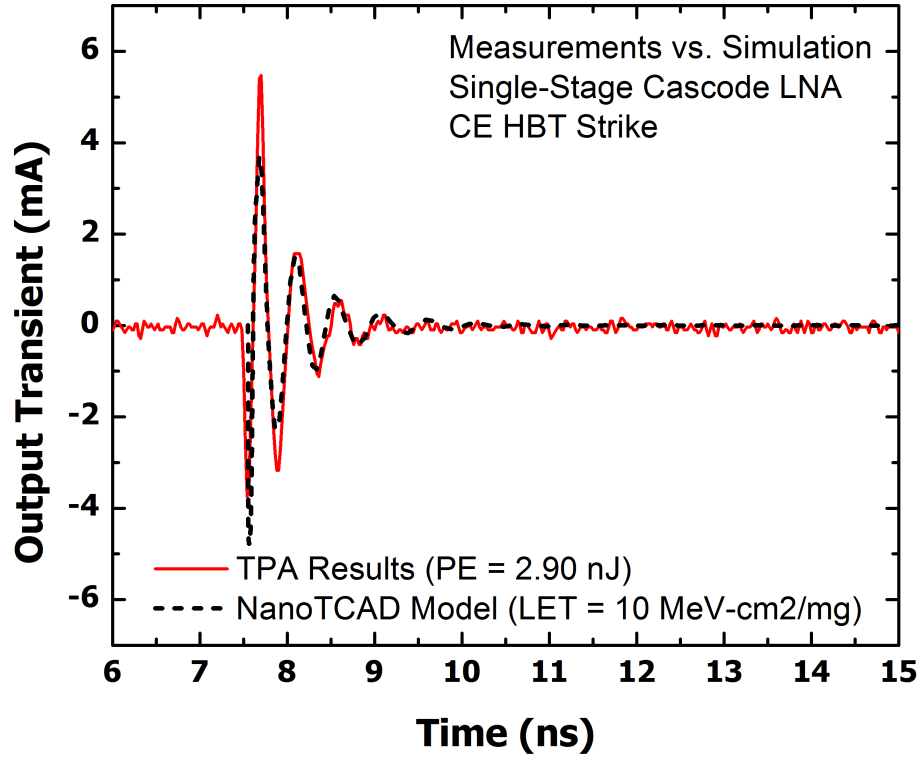


Figure 4.6: Comparison of simulation to measured transient at the output of the LNA with the FF configuration.

to measured SET data taken from [41]. (The reader is also referred to this study for the specific measurement setup using pulsed-lasers to induce SETs.) Fig. 4.6 shows the laser-induced measured transient (solid red line) compared to the resulting transient from the mixed-mode simulation setup (black dashed line). The simulation was performed using the FF cascode variant that was in Fig. 4.5 to mimic the same setup with the measurement. The circuit was also biased identically to the experimental setup. The data show excellent agreement between simulation and measurement, which makes this simulation setup more robust and reliable when various parameters are changed, e.g. temperature.

One thing to note is that this circuit transient looks very different than the single device transient. The decaying sinusoidal shape can be explained from the fact that an SET can be thought of as an impulse in the device. As the transient propagates from Q1 and out of



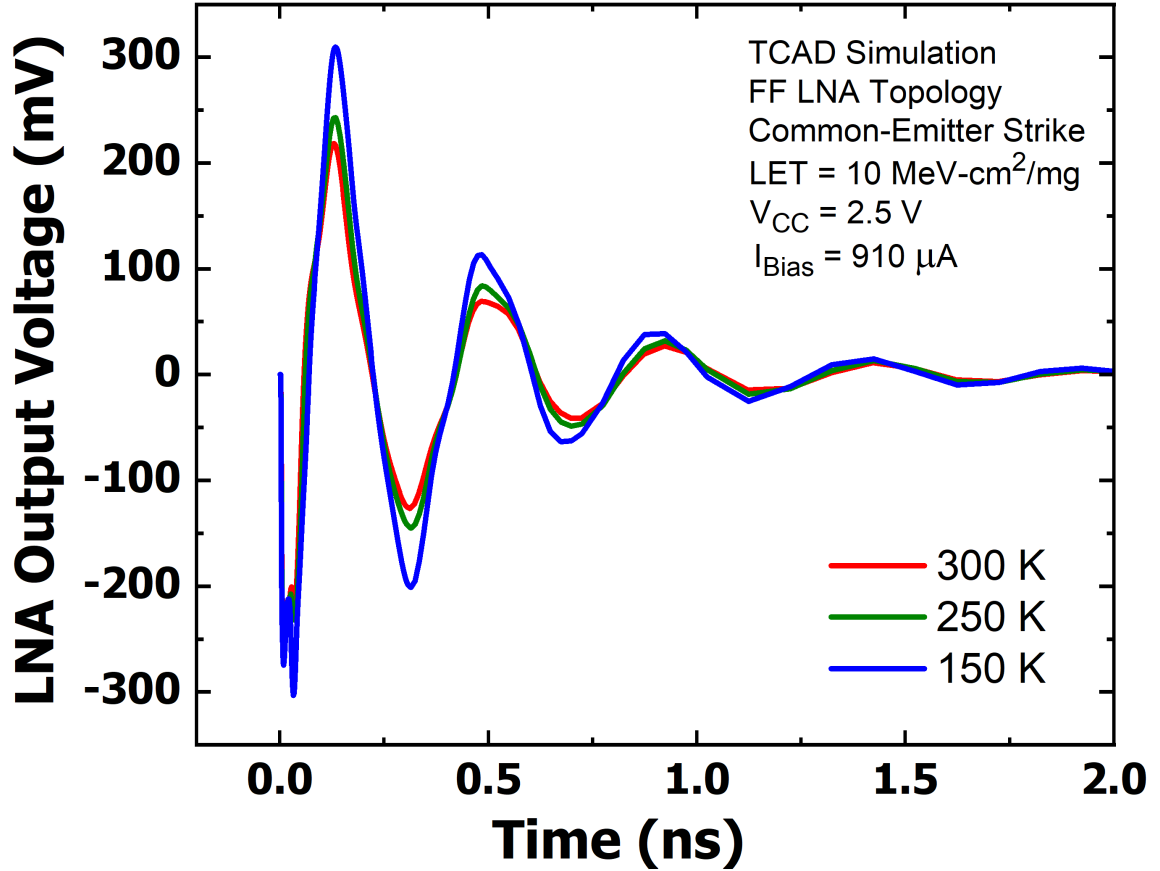


Figure 4.7: Output voltage of the LNA as Q1 is struck with LET = 10 MeV-cm<sup>2</sup>/mg for 300, 250, and 150 K.

Q2, it is faced with the output matching network of the circuit. Since this is a narrowband 2.4 GHz LNA, the transient is shaped around 2.4 GHz at the output. Another way to think of the output matching network is a passive filter. The impulse response of the filter does look like a 2.4 GHz decaying sinusoid.

With this in mind, it is desirable to understand if and how the shape of this transient changes with varying temperature. Fig. 4.7 shows the simulation results for the LNA with the FF variant across 3 different temperatures. As the temperature of the circuit decreases it is clear that the absolute magnitude of the transient increases. This is in agreement with the single device transients. However, the duration does not change by any significant amount.

To understand this phenomenon a little deeper, the collector current of the CE device was probed and the currents were recorded. The result is shown in Fig. 4.8. According

to the simulation, up to about 20 ps the transient shape and trend resemble that of the single device transient. However, within the circuit context, there seems to be a rebound that produces a second peak. This is most likely due to the circuit itself trying to back to equilibrium. The important part of this data is that all of the transient action happens within the first 70-80 ps after which the transient dies down. The CE transient is much shorter than the circuit transients observed in Fig. 4.7. This means that the duration of the circuit transient on its output is decoupled from the transient physics that are happening within the device itself. In other words, the peak magnitude of the transient in the CE device that results from the heavy-ion strike sets the initial condition of the decaying sinusoid response of the circuit. Once the CE transient ends after 70-80 ps, the circuit responds as if it were an impulse and then continues to oscillate at 2.4 GHz until the circuit reaches equilibrium.

One last thing to note is that this double peak in the CE response actually shows up in the overall circuit transient within the first peak in Fig. 4.7. The relevance of this, however, cannot be determined whether it is a negative or negligible effect since these transients are not in the context of data, so it is difficult to say whether or not any data will be corrupted.

#### *Inverse Mode Operation (IF and II)*

As mentioned earlier, inverse mode can be used as a technique for RHBD in RF circuits to decrease the impact of a heavy-ion strike on the circuit as well as decrease the sensitive area of the circuit that is prone to respond negatively from heavy-ion strikes. The question is, does cooling the circuit help or hurt this RHBD technique?

Shown in Figs. 4.9 and 4.10 is a collection of simulation results showing LNA output voltage and the CE collector current, respectively, for 300, 250, and 150 K comparing FF, IF, and II LNA configurations. All of the axes are on the same scale for ease of comparison and Fig. 4.10 has gray lines and arrows for references. It is clear from the simulation data that the II configuration does exhibit the smallest transient peak across all temperatures. It is also worthy to note that while the transient magnitude in output voltage for all of the

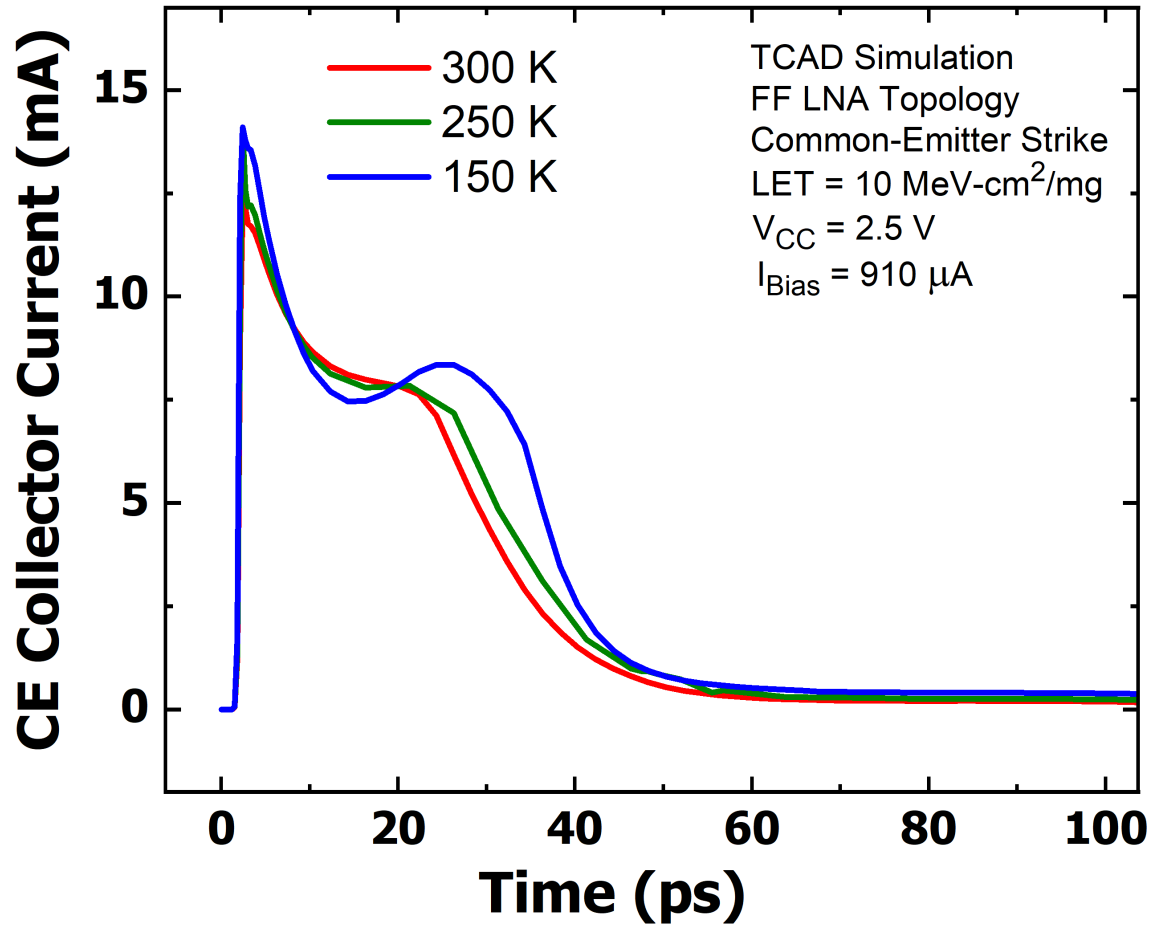


Figure 4.8: Collector current of the CE device (Q1) as Q1 is struck with LET = 10 MeV-cm<sup>2</sup>/mg for 300, 250, and 150 K.

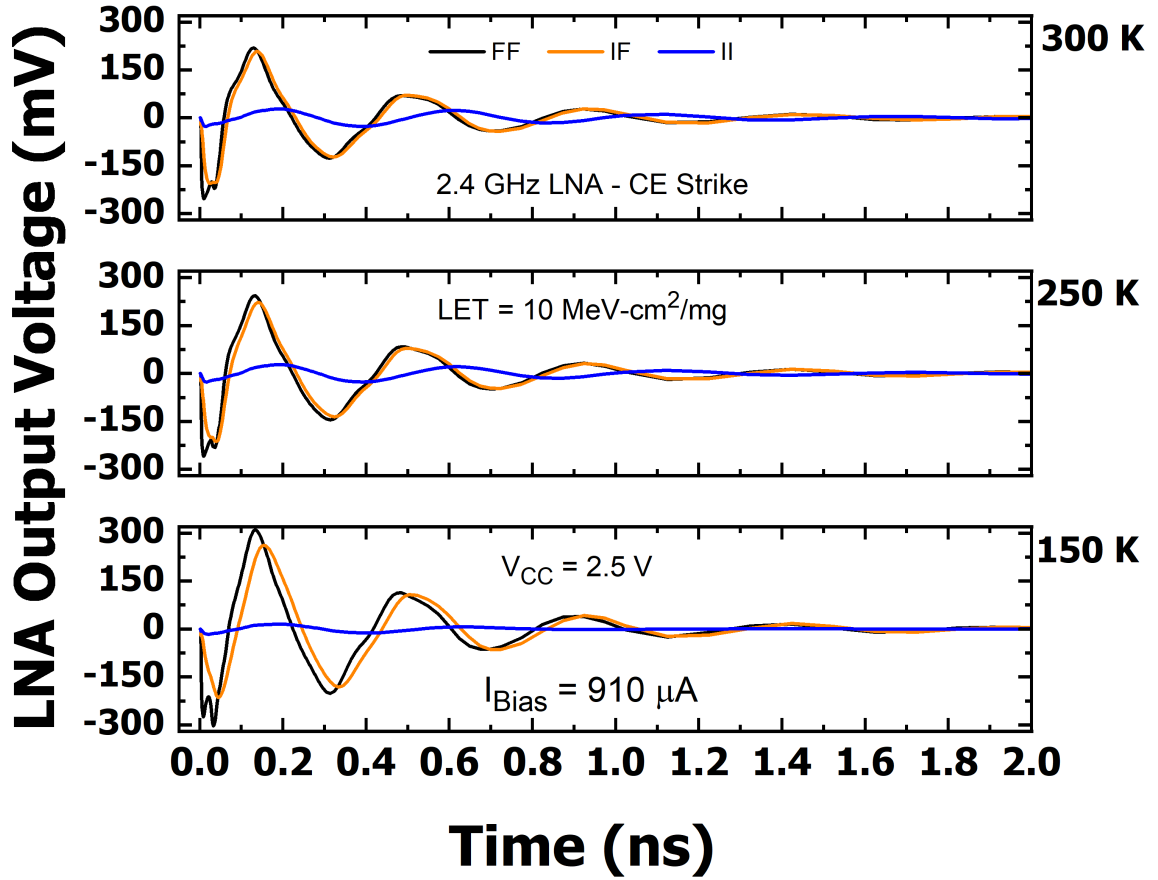


Figure 4.9: Output voltage of the LNA as Q1 is struck with LET = 10 MeV-cm<sup>2</sup>/mg for 300, 250, and 150 K with FF, IF, and II topologies. Note that all of the axis are on the same scale.

configurations increases when temperature is decreased, the magnitude of the transients in the IF configuration increase at a slower rate than the transients in the FF configuration. This is clearly a good thing as the IF configuration does show an improvement in SET vulnerability. The last thing to note is that it seems like there are frequency variations with all of the configurations. This is attributed to the fact that the input and output impedances of the circuit are being altered from the fact that the SiGe HBTs are being flipped. The most notable difference in frequency is in the II configuration where it seems like the frequency of operation of the circuit has decreased in value. This means that when using inverse mode, careful attention must be placed on the input and output matching networks to be able maximize the performance of the circuit.

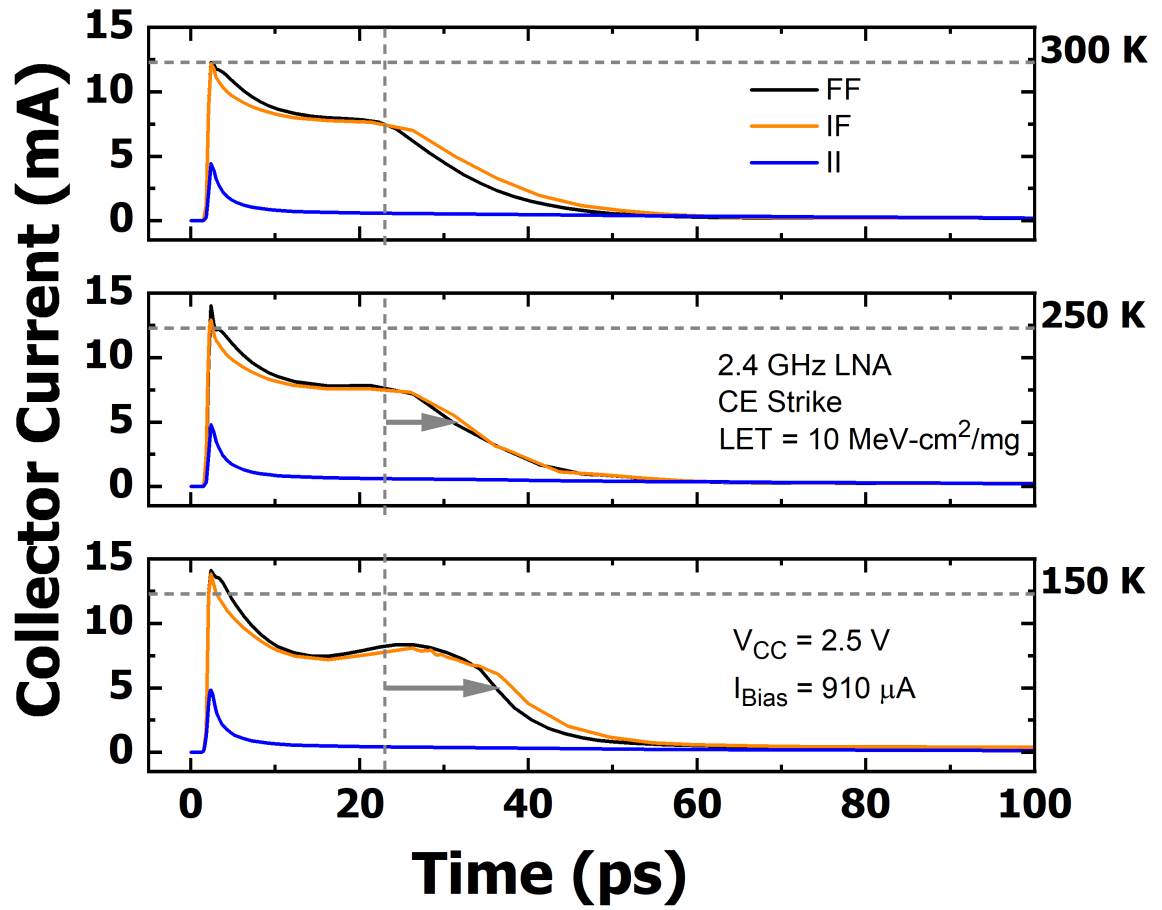


Figure 4.10: CE Collector current of the LNA as Q1 is struck with LET = 10 MeV-cm<sup>2</sup>/mg for 300, 250, and 150 K with FF, IF, and II topologies. Dashed gray lines and solid arrows are displayed as references for the reader to see relative magnitudes between the stacked plots.

## 4.4 Discussion

While SET analysis in terms of magnitude, duration, and collected charge is good to be studied on a single device level, it has little meaning until those metrics are put in terms of how each affects the primary functionality of the circuit, e.g. bit error rate. In this simulation study, it was shown that the single device transient increases in magnitude but decreases in duration when cooled. However, in the circuit simulations it was shown that the CE transient peak was the main parameter that influenced the magnitude of the output voltage transient of the circuit. This is clearly not a desirable thing for this circuit if it is to operate in cold environments. In other words, cold temperatures make the transient response of this LNA worse.

However, it is clear that the inverse mode technique works well in reducing the circuit transient because it specifically reduces the CE transient peak. The reduction in the circuit transient peak will have a direct impact on reducing data errors that would pass through an LNA like this. If the signal's data was encoded in the amplitude of the signal, then clearly a smaller transient peak would help with reducing the number of errors due to the transient. Furthermore, if the data was encoded in the phase of the signal, a transient in the circuit could cause the signal to become too small, or distorted, such that the data would be corrupted. So reducing the peak with inverse mode would be worth the pursuit. Future work on this topic is needed with simulations and measurements to quantify to what extent these transients could affect the data that is going through the LNA, and how the data rate affects the probability of errors.

The opposite case could also be true, namely that the transient duration affects the circuit response rather than the transient peak. In a simulation study done by Xu et al [48] the authors noticed that with a CML master-slave D-flip-flop a decrease in the temperature of operation of the circuit actually improves the overall circuit performance and shows less errors. The authors attribute this to the much shorter transient duration that happens at the

device level at lower temperatures. In this case, the transient duration is the driving factor that determines the circuit response. So the D-flip-flop circuit would be more resilient to SEEs at low temperatures.

It is important for designers who are considering various RHBD techniques for space missions to know which feature (refer to Fig. 1.9) of the transient they are trying to suppress. For the LNA case, it was shown that reduction in the peak using inverse mode works well. For the D-flip-flop case, using something like an SOI platform as an RHBD technique to decrease the duration of the transient at lower temperatures would be an ideal candidate [38].

#### **4.5 Summary and Future Work**

SETs at low temperatures were shown to increase the peak of a single-device transient in a SiGe HBT but reduce the duration. The impact of both of these trends on a circuit/system level very heavily depends on the circuit/system in question. For the cascode LNA, it was shown that the transient response of the circuit is worse at colder temperatures and could cause issues in bit errors if proper attention is not given. RHBD techniques, such as inverse mode configurations, to decrease the amplitude of the device transient where the SET originates will mitigate this issue at lower temperatures. On the other hand, for circuits like the CML D-flip-flop, it was shown that the transient response actually gets better at lower temperatures due to the decrease in the device transient duration. Again, RHBD techniques that specifically reduce the transient duration, like using an SOI platform, could be used to mitigate the transient effects on the system even more. In summary, the SET impact on various circuit blocks with decreasing temperature varies with the functionality of the circuit. While some circuits will exhibit worse SET effects at colder temperatures, others will gain an intrinsic benefit in operating at those low temperatures. Designers who wish to utilize RHBD techniques must consider which part of the transient they are wanting to reduce. This will drive their design efforts to trade off minimal circuit performance for

maximum SET mitigation.

Future work on this topic should include evaluating the SET response over temperature on various circuit/system blocks such as RF switches, mixers, power amplifiers, etc. Each of those building blocks should incorporate an analysis about which transient feature within the device is driving factor for the overall circuit/system transient, and how that transient might affect the main functionality of the block in question. Once the SET response at low temperatures for these blocks is defined, designers can build the next generation of electronics that would be highly reliable for space missions that exhibit both low temperatures and heavy-ion radiation, e.g. missions to Europa.



## **CHAPTER 5**

### **CONCLUSION**

#### **5.1 Contributions**

This thesis has demonstrated that SiGe technology is a strong contender for low temperature, high radiation environments with some caveats. From a TID perspective, the SiGe HBT shows high resiliency at low temperatures when irradiated to high doses. On the other hand, from an SEE perspective, the SiGe HBT does show an increased vulnerability at lower temperatures when used in circuits that are sensitive to transient amplitudes. However, when the SiGe HBT is used in circuits that are sensitive to the transient tail they show less vulnerability. While more research needs to be conducted to experimentally validate chapter 4 of this thesis, the data shown is a good indicator that SiGe HBTs can be used for deep-space applications.

#### **5.2 Future Work**

There are still many questions regarding the response to TID and SEE of different system block diagrams that incorporate SiGe technology. For instance, this thesis only showed the low-temperature radiation response of an LNA. While suggesting that other circuits will also not degrade with low-temperature TID, experiments to validate this claim need to be done. The same could be said for low-temperature SEEs in that experimental validation for different circuit/system blocks utilizing SiGe HBTs needs to be done.

## REFERENCES

- [1] M. Xapsos, “A brief history of space climatology: From the big bang to the present,” *IEEE Transactions on Nuclear Science*, vol. 66, no. 1, pp. 17–37, 2019.
- [2] J. J. Cowan and C. Sneden, “Heavy element synthesis in the oldest stars and the early universe,” *Nature*, vol. 440, no. 7088, pp. 1151–1156, 2006.
- [3] E. Anders and N. Grevesse, “Abundances of the elements: Meteoritic and solar,” *Geochimica et Cosmochimica Acta*, vol. 53, no. 1, pp. 197–214, 1989.
- [4] R. A. Mewaldt, “Galactic cosmic ray composition and energy spectra,” *Advances in Space Research*, vol. 14, no. 10, pp. 737–747, 1994.
- [5] E. J. Daly, J. Lemaire, D. Heynderickx, and D. J. Rodgers, “Problems with models of the radiation belts,” *IEEE Transactions on Nuclear Science*, vol. 43, no. 2 PART 1, pp. 403–415, 1996.
- [6] E. Roussos, P. Kollmann, N. Krupp, A. Kotova, L. Regoli, C. Paranicas, D. G. Mitchell, S. M. Krimigis, D. Hamilton, P. Brandt, J. Carbary, S. Christon, K. Dialynas, I. Dandouras, M. E. Hill, W. H. Ip, G. H. Jones, S. Livi, B. H. Mauk, B. Palmaerts, E. C. Roelof, A. Rymer, N. Sergis, and H. T. Smith, “A radiation belt of energetic protons located between Saturn and its rings,” *Science*, vol. 362, no. 6410, 2018.
- [7] T. I. Gombosi, T. P. Armstrong, C. S. Arridge, K. K. Khurana, S. M. Krimigis, N. Krupp, A. M. Persoon, and M. F. Thomsen, “Saturn’s magnetospheric configuration,” in *Saturn from Cassini-Huygens*, M. K. Dougherty, L. W. Esposito, and S. M. Krimigis, Eds. Dordrecht: Springer Netherlands, 2009, pp. 203–255, ISBN: 978-1-4020-9217-6.
- [8] C. Russell, “The dynamics of planetary magnetospheres,” *Planetary and Space Science*, vol. 49, no. 10, pp. 1005–1030, 2001, Magnetosphere of the Outer Planets Part II.
- [9] H. Garrett, I. Jun, R. Evans, W. Kim, and D. Brinza, “The Latest Jovian-Trapped Proton and Heavy Ion Models,” *IEEE Transactions on Nuclear Science*, vol. 64, no. 11, pp. 2802–2813, 2017.
- [10] J. R. Srour, C. J. Marshall, and P. W. Marshall, “Review of displacement damage effects in silicon devices,” *IEEE Transactions on Nuclear Science*, vol. 50 III, no. 3, pp. 653–670, 2003.

- [11] J. R. Srouf and J. W. Palko, "Displacement damage effects in irradiated semiconductor devices," *IEEE Transactions on Nuclear Science*, vol. 60, no. 3, pp. 1740–1766, 2013.
- [12] D. Kobayashi, "Basics of Single Event Effect Mechanisms and Predictions," *IEEE Nuclear and Space Radiation Effects Conf. Short Course*, 2019, San Antonio, TX.
- [13] R. C. Baumann, "Single-Event Effects in Advanced CMOS Technology," *IEEE Nuclear and Space Radiation Effects Conf. Short Course*, 2005, Seattle, WA.
- [14] A. Ildefonso, Z. E. Fleetwood, G. N. Tzintzarov, J. M. Hales, D. Nergui, M. Frounchi, A. Khachatrian, S. P. Buchner, D. McMorro, J. H. Warner, J. Harms, A. Erickson, K. Voss, V. Ferlet-Cavrois, and J. D. Cressler, "Optimizing Optical Parameters to Facilitate Correlation of Laser-and Heavy-Ion-Induced Single-Event Transients in SiGe HBTs," *IEEE Transactions on Nuclear Science*, vol. 66, no. 1, pp. 359–367, 2019.
- [15] F. B. McLean and T. R. Oldham, "Basic mechanisms of radiation effects in electronic materials and devices.," *Harry Diamond Laboratories*, Sep. 1987.
- [16] D. M. Fleetwood, "Total ionizing dose effects in MOS and low-dose-rate-sensitive linear-bipolar devices," *IEEE Transactions on Nuclear Science*, vol. 60, no. 3, pp. 1706–1730, 2013.
- [17] H. J. Barnaby, M. L. McLain, I. S. Esqueda, and X. J. Chen, "Modeling ionizing radiation effects in solid state materials and CMOS devices," *2008 IEEE Custom Integrated Circuits Conference*, vol. 56, no. 8, pp. 273–280, 2008.
- [18] J. Cressler and G. Niu, "Silicon-germanium heterojunction bipolar transistors," Jan. 2003.
- [19] GlobalFoundries SiGe HP Technologies, [ONLINE]. Available: <https://www.globalfoundries.com/technologies/rf-soi-and-sige-technologies/sige-hp-technologies>.
- [20] J. Cressler, "On the Potential of SiGe HBTs for Extreme Environment Electronics," *Proceedings of the IEEE*, vol. 93, no. 9, pp. 1559–1582, 2005.
- [21] J. D. Cressler, "Radiation Effects in SiGe Technology," *IEEE Transactions on Nuclear Science*, vol. 60, no. 3, pp. 1992–2014, 2013.
- [22] N. E. Lourenco, R. L. Schmid, K. A. Moen, S. D. Phillips, T. D. England, J. D. Cressler, J. Pekarik, J. Adkisson, R. Camillo-Castillo, P. Cheng, J. E. Monaghan, P. Gray, D. Harame, M. Khater, Q. Liu, A. Vallett, B. Zetterlund, V. Jain, and V. Kaushal, "Total dose and transient response of SiGe HBTs from a new 4th-

generation, 90 nm SiGe BiCMOS technology,” *IEEE Radiation Effects Data Workshop*, pp. 4–8, 2012.

- [23] J. L. Barth, “Space and atmospheric environments: From low earth orbits to deep space,” *European Space Agency, (Special Publication) ESA SP*, no. 540, pp. 17–30, 2003.
- [24] N. E. Lourenco, Z. E. Fleetwood, A. Ildefonso, M. T. Wachter, N. J. Roche, A. Khachatryan, D. McMorrow, S. P. Buchner, J. H. Warner, H. Itsuji, D. Kobayashi, K. Hirose, P. Paki, A. Raman, J. D. Cressler, S. S. Member, A. Ildefonso, S. S. Member, M. T. Wachter, S. S. Member, N. J. Roche, A. Khachatryan, D. McMorrow, S. S. Member, S. P. Buchner, J. H. Warner, H. Itsuji, D. Kobayashi, K. Hirose, P. Paki, A. Raman, and J. D. Cressler, “The Impact of Technology Scaling on the Single-Event Transient Response of SiGe HBTs,” *IEEE Transactions on Nuclear Science*, vol. 64, no. 1, pp. 406–414, 2017.
- [25] A. Ildefonso, I. Song, Z. E. Fleetwood, N. E. Lourenco, M. T. Wachter, G. N. Tzintzarov, and J. D. Cressler, “Modeling single-event transient propagation in a SiGe BiCMOS direct-conversion receiver,” *Proceedings of the European Conference on Radiation and its Effects on Components and Systems, RADECS*, vol. 2016-September, no. 8, pp. 1–5, 2017.
- [26] N. E. Lourenco, A. Ildefonso, G. N. Tzintzarov, Z. E. Fleetwood, K. Motoki, P. Paki, M. Kaynak, and J. D. Cressler, “Single-Event Upset Mitigation in a Complementary SiGe HBT BiCMOS Technology,” *IEEE Transactions on Nuclear Science*, vol. 65, no. 1, pp. 231–238, 2018.
- [27] G. N. Tzintzarov, A. Ildefonso, P. S. Goley, M. Frounchi, D. Nergui, S. G. Rao, J. Teng, J. Campbell, A. Khachatryan, S. P. Buchner, D. McMorrow, J. H. Warner, M. Kaynak, L. Zimmermann, and J. D. Cressler, “Electronic-to-photon single-event transient propagation in a segmented machzehnder modulator in a si/sige integrated photonics platform,” *IEEE Transactions on Nuclear Science*, vol. 67, no. 1, pp. 260–267, 2020.
- [28] P. S. Chakraborty, A. S. Cardoso, B. R. Wier, A. P. Omprakash, J. D. Cressler, M. Kaynak, and B. Tillack, “A 0.8 thz  $f_{\max}$  si/sige hbt operating at 4.3 k,” *IEEE Electron Device Letters*, vol. 35, no. 2, pp. 151–153, 2014.
- [29] A. S. Cardoso, A. P. Omprakash, P. S. Chakraborty, N. Karaulac, D. M. Fleischhauer, A. Ildefonso, S. Zeinolabedinzadeh, M. A. Oakley, T. G. Bantu, N. E. Lourenco, and J. D. Cressler, “On the Cryogenic RF Linearity of SiGe HBTs in a Fourth-Generation 90-nm SiGe BiCMOS Technology,” *IEEE Transactions on Electron Devices*, vol. 62, no. 4, pp. 1127–1135, 2015.

- [30] H. Ying, B. R. Wier, J. Dark, N. E. Lourenco, L. Ge, A. P. Omprakash, M. Mourigal, D. Davidovic, and J. D. Cressler, "Operation of SiGe HBTs down to 70 mK," *IEEE Electron Device Letters*, vol. 38, no. 1, pp. 12–15, 2017.
- [31] A. H. Johnston, R. T. Swimm, and D. O. Thorbourn, "Charge Yield at Low Electric Fields: Considerations for Bipolar Integrated Circuits," *IEEE Transactions on Nuclear Science*, vol. 60, no. 6, pp. 4488–4497, 2013.
- [32] H. J. Barnaby, "Total-Ionizing-Dose Effects in Modern CMOS Technologies," *IEEE Transactions on Nuclear Science*, vol. 53, no. 6, pp. 3103–3121, 2006.
- [33] A. Raman, M. Turowski, A. Fedoseyev, and J. D. Cressler, "Addressing challenges in device-circuit modeling for extreme environments of space," *2007 International Semiconductor Device Research Symposium, ISDRS*, pp. 12–13, 2007.
- [34] M. Turowski, A. Fedoseyev, A. Raman, and K. Warren, "Single event upset modeling with nuclear reactions in nanoscale electronics," *Proceedings of The 15th International Conference Mixed Design of Integrated Circuits and Systems, MIXDES 2008*, vol. 4, pp. 443–448, 2008.
- [35] A. Fedoseyev, R. Arslanbekov, and M. Turowski, "Simulations of complex nuclear events from high energy ion tracks in integrated circuits with 3D NanoTCAD," *2010 14th International Workshop on Computational Electronics, IWCE 2010*, pp. 77–80, 2010.
- [36] N. D. Arora, J. R. Hauser, and D. J. Roulston, "Electron and Hole Mobilities in Silicon as a Function of Concentration and Temperature," *IEEE Transactions on Electron Devices*, vol. 29, no. 2, pp. 292–295, 1982.
- [37] P. Zheng, F. E. Rougieux, D. Macdonald, and A. Cuevas, "Parameterization of carrier mobility sum in silicon as a function of doping, temperature and injection level: Extension to p-type silicon," *2014 IEEE 40th Photovoltaic Specialist Conference, PVSC 2014*, vol. 4, no. 2, pp. 129–134, 2014.
- [38] A. Ildefonso, G. N. Tzintzarov, A. P. Omprakash, D. Nergui, P. Goley, J. M. Hales, A. Khachatrian, S. P. Buchner, D. Mcmorrow, J. H. Warner, J. D. Cressler, and A. Ildefonso, "Comparison of Single-Event Transients in SiGe HBTs on Bulk and Thick-Film SOI," *IEEE Transactions on Nuclear Science*, vol. 67, no. 1, pp. 71–80, 2020.
- [39] Z. E. Fleetwood, N. E. Lourenco, A. Ildefonso, J. H. Warner, M. T. Wachter, J. M. Hales, G. N. Tzintzarov, N. J. Roche, A. Khachatrian, S. P. Buchner, D. Mc Morrow, P. Paki, and J. D. Cressler, "Using TCAD Modeling to Compare Heavy-Ion and Laser-Induced Single Event Transients in SiGe HBTs," *IEEE Transactions on Nuclear Science*, vol. 64, no. 1, pp. 398–405, 2017.

- [40] Spectre Simulation Platform, [ONLINE]. Available: [https://www.cadence.com/en\\_US/home/tools/custom-ic-analog-rf-design/circuit-simulation/spectre-simulation-platform.html](https://www.cadence.com/en_US/home/tools/custom-ic-analog-rf-design/circuit-simulation/spectre-simulation-platform.html).
- [41] I. Song, M. K. Cho, N. E. Lourenco, Z. E. Fleetwood, S. Jung, N. J. Roche, A. Khachatrian, S. P. Buchner, D. McMorrow, P. Paki, and J. D. Cressler, "The use of inverse-mode SiGe HBTs as active gain stages in low-noise amplifiers for the mitigation of single-event transients," *IEEE Transactions on Nuclear Science*, vol. 64, no. 1, pp. 359–366, 2017.
- [42] I. Song, M. K. Cho, M. A. Oakley, A. Ildefonso, I. Ju, S. P. Buchner, D. McMorrow, P. Paki, and J. D. Cressler, "On the Application of Inverse-Mode SiGe HBTs in RF Receivers for the Mitigation of Single-Event Transients," *IEEE Transactions on Nuclear Science*, vol. 64, no. 5, pp. 1142–1150, 2017.
- [43] S. D. Phillips, K. A. Moen, N. E. Lourenco, and J. D. Cressler, "Single-event response of the SiGe HBT operating in inverse-mode," *IEEE Transactions on Nuclear Science*, vol. 59, no. 6, pp. 2682–2690, 2012.
- [44] N. E. Lourenco, S. D. Phillips, T. D. England, A. S. Cardoso, Z. E. Fleetwood, K. A. Moen, D. McMorrow, J. H. Warner, S. P. Buchner, P. Paki-Amouzou, J. Pekarik, D. Hameed, A. Raman, M. Turowski, and J. D. Cressler, "An investigation of single-event effects and potential seu mitigation strategies in fourth-generation, 90 nm sige bicmos," *IEEE Transactions on Nuclear Science*, vol. 60, no. 6, pp. 4175–4183, 2013.
- [45] Z. E. Fleetwood, A. Ildefonso, G. N. Tzintzarov, B. Wier, U. Raghunathan, M. K. Cho, I. Song, M. T. Wachter, D. Nergui, A. Khachatrian, J. H. Warner, P. McMarr, H. Hughes, E. Zhang, D. McMorrow, P. Paki, A. Joseph, V. Jain, and J. D. Cressler, "SiGe HBT Profiles with Enhanced Inverse-Mode Operation and Their Impact on Single-Event Transients," *IEEE Transactions on Nuclear Science*, vol. 65, no. 1, pp. 399–406, 2018.
- [46] I. Song, U. S. Raghunathan, N. E. Lourenco, Z. E. Fleetwood, M. A. Oakley, S. Jung, M. K. Cho, N. J. Roche, A. Khachatrian, J. H. Warner, S. P. Buchner, D. McMorrow, P. Paki, and J. D. Cressler, "An Investigation of the Use of Inverse-Mode SiGe HBTs as Switching Pairs for SET-Mitigated RF Mixers," *IEEE Transactions on Nuclear Science*, vol. 63, no. 2, pp. 1099–1108, 2016.
- [47] S. D. Phillips, T. Thrivikraman, A. Appaswamy, A. K. Sutton, J. D. Cressler, G. Vizkelethy, P. Dodd, and R. A. Reed, "A novel device architecture for SEU mitigation: The inverse-mode cascode SiGe HBT," *IEEE Transactions on Nuclear Science*, vol. 56, no. 6, pp. 3393–3401, 2009.

- [48] Z. Xu, G. Niu, L. Luo, J. D. Cressler, M. L. Alles, R. Reed, H. A. Mantooth, J. Holmes, and P. W. Marshall, "Charge collection and SEU in SiGe HBT current mode logic operating at cryogenic temperatures," *IEEE Transactions on Nuclear Science*, vol. 57, no. 6 PART 1, pp. 3206–3211, 2010.